Coherent structures, instabilities, and turbulence in interfacial and magnetohydrodynamic flows

Zusammenfassung wissenschaftlicher Veröffentlichungen

zur Erlangung des akademischen Grades

Doctor rerum naturalium habilitatus (Dr. rer. nat. habil.)

vorgelegt der
Fakultät für Maschinenbau der
Technischen Universität Ilmenau

von Herrn
Dr. rer. nat. Thomas Boeck
geboren am 16. 3. 1970 in Meißen

urn:nbn:de:gbv:ilm1-2010200133

Datum der Einreichung: 8. 6. 2009
Datum der Probevorlesung: 6. 1. 2010
Datum des wissenschaftlichen Vortrags mit Kolloquium: 15. 3. 2010
Vollzug der Habilitation: 20. 4. 2010

Mitglieder der Habilitationskommission:

Univ.-Prof. Dr.-Ing. habil. Peter Kurtz, TU Ilmenau, Vorsitzender der Kommission
Univ.-Prof. Dr. rer. nat. habil. Jörg Schumacher, TU Ilmenau, Gutachter
Univ.-Prof. Dr. rer. nat. habil. Hendrik Kuhlmann, TU Wien, Gutachter
Prof. Dr. Bernard Knaepen, Université Libre de Bruxelles, Gutachter
Univ.-Prof. Dr. rer. nat. habil. André Thess, TU Ilmenau
Univ.-Prof. Dr. rer. nat. habil. Stefan Sinzinger, TU Ilmenau

Zusammenfassung

Die vorliegende Arbeit stellt die Beiträge des Autors zu mehreren theoretischen und numerischen Untersuchungen von Instabilitäten und komplexer nichtlinearer Dynamik in Strömungen vor. Bei den betrachteten Strömungen handelt es sich um thermische Konvektion in Ein- und Zwei-Schicht-Systemen nichtmischbarer Fluide, Zweiphasen-Scherschichten und Kanalströmungen elektrisch leitfähiger Flüssigkeiten in einem äußeren Magnetfeld. Diese Konfigurationen sind durch eine Reihe von Anwendungen motiviert, z.B. Wärme- und Stoffübergang an fluiden Grenzflächen bei verfahrenstechnischen Prozessen, Zerstäubung von Flüssigkeiten für die Verbrennung oder elektromagnetische Pumpen und Bremsen für die Materialverarbeitung in der Metallurgie. Die Komplexität der realen Anwendungen wurde beträchtlich reduziert, um fundamentale Mechanismen und Eigenschaften solcher Strömungen zu untersuchen. Die erreichte geometrische und konzeptionelle Einfachheit ist zweckmäßig für die numerischen Untersuchungen, weil man dadurch spezialisierte, aber sehr effiziente numerische Methoden einsetzen kann. Die Ergebnisse solcher Untersuchungen können das physikalische Verständnis der Strömungen verbessern und zur Validierung von allgemeineren numerischen Verfahren dienen.

Auf dem Gebiet der thermischen Konvektion hat der Autor mehrere Anordnungen untersucht. Die erste ist oberflächenspannungsgetriebene (thermokapillare) Konvektion in einer einzelnen Flüssigkeitsschicht. Für diese Anordunung wurden die Strömungsstruktur und das Skalierungsverhalten des Wärmestroms mit zwei- und dreidimensionalen Simulationen untersucht, einschließlich des Falls mit Magnetfeld. Die Kopplung zwischen thermokapillarer Strömung und Auftrieb spielt in einen System aus zwei Schichten mit Heizung von unten eine Rolle. Diese Anordnung kann eine oszillatorische Instabilität des wärmeleitenden Grundzustands aufweisen sowie eine Reihe verschiedener möglicher Konvektionsmuster für deren nichtlineare Sättigung. In einer weiteren Zwei-Schicht-Anordnung führt die thermische und mechanische Kopplung an der Grenzfläche zwischen Flüssigkeitsschichten mit sehr unterschiedlichen Wärmeleitfähigkeiten zu einer auftriebsinduzierten Instabilität bei Heizung von oben. Diese beiden Zwei-Schicht-Systeme wurden mit dreidimensionalen, nichtlinearen Simulationen untersucht, wobei der Schwerpunkt auf den Veränderungen der Konvektionsmuster bei Variation der Stärke des thermischen Antriebs lag.

Auf dem Gebiet der Zweiphasen-Scherschichten hat der Autor zwei lineare Stabilitätsuntersuchungen auf der Grundlage der gekoppelten Rayleigh/Orr-Sommerfeld-Gleichungen durchgeführt, sowie eine Verifikation des nichtlinearen SURFER Codes mit Hilfe der linearen Stabilitätsresultate aus den Orr-Sommerfeld-Gleichungen. Das Neue an diesen Arbeiten ist der direkte Vergleich der Resultate für den reibungsfreien Fall und den Fall endlicher Zähigkeit bei Grundströmungen mit gleicher Struktur, und die Identifikation eines spezifischen, zähigkeitsbedingten Instabilitätsmechanismus im Parameterbereich von Zerstäubungsexperimenten mit Luft und Wasser. Weiterhin wurde die Gültigkeit bestimmter Näherungen für das Geschwindigkeitsprofil der Grundströmung mit Hilfe exakter Lösungen der Grenzschichtgleichungen für zwei Fluide

bestätigt.

Auf dem Gebiet der Kanalströmungen leitfähiger Flüssigkeiten war der Autor an numerischen Untersuchungen des Turbulenzübergangs und der Turbulenz beteiligt. Für ein Magnetfeld in Spannweitenrichtung wurde ein nichtlinearer Mechanismus für den Turbulenzübergang bei subkritischer Reynoldszahl analysiert. Außerdem wurden die Eigenschaften der Turbulenz sowohl für ein Magnetfeld senkrecht zur Kanalwand als auch mit Magnetfeld in Spannweitenrichtung mittels numerischer Simulationen bestimmt. Zusätzlich wurde die Eignung des dynamischen Smagorinsky-Modells für die Grobstruktursimulation solcher Strömungen durch Vergleich mit direkten numerischen Simulationen nachgewiesen.

Die Zusammenfassung schildert vorwiegend die Motivation für die verschiedenen Arbeiten sowie die grundlegende Physik der betrachteten Strömungen. Hauptergebnisse werden auch angegeben. Einzelheiten zu den mathematischen Modellen und numerischen Methoden finden sich in den Veröffentlichungen. Der Eigenanteil des Autors an den verschiedenen Veröffentlichungen ist in einem separaten Anhang ausgewiesen.

Contents

1 Introduction

The present work outlines the contributions of the author to several theoretical and numerical investigations of instabilities and complex nonlinear dynamics in fluid flows. The flows under study are thermal convection in single and immiscible double fluid layers, two-phase shear layers, and channel flows of electrically conducting fluid with an imposed magnetic field. These configurations are motivated by a variety of applications, e.g. interfacial heat and mass transfer in chemical engineering processes, liquid atomization for combustion, or electromagnetic pumps and brakes for the processing of materials in metallurgy. The complexity of the real applications has been reduced considerably in order to examine fundamental mechanisms and properties. The geometric and conceptual simplicity achieved this way is also useful for the numerical studies since it typically allows one to use specialized but very efficient simulation methods. The results of such investigations can improve our understanding of flow physics and can also serve as benchmarks for the verification of more general computational approaches.

On the topic of thermal convection the author has considered several configurations. The first is purely surface-tension driven convection in a single liquid layer. For this configuration the flow structure and the heat flux scaling was studied by two-dimensional and three-dimensional simulations, and in the presence of a magnetic field. The coupling between thermocapillary and buoyancy convection plays a role in a system of two coupled layers heated from below. This configuration admits an oscillatory instability of the basic state of pure heat conduction, and a variety of possible convective patterns for the nonlinear saturation of this instability. In another two-layer configuration, the thermal and mechanical coupling between layers of very different thermal conductivity gives rise to a buoyancy-induced instability with heating from above. These two systems were studied by three-dimensional numerical simulations in the nonlinear regime with a focus on the transformation of the convective patterns with the thermal forcing.

On the topic of two-phase mixing layers the author has performed two linear stability studies based on coupled Rayleigh/Orr-Sommerfeld equations, and a verification of the nonlinear simulation code SURFER by means of the viscous linear stability results. The novelty in the linear stability calculations consisted in a direct comparison of viscous and inviscid results for geometrically equivalent configurations, and in the identification of a specific viscous instability mechanism in the parameter range of experiments on air/water atomization. Moreover, the validity of certain approximate velocity profiles of the basic flow was studied by means of exact solutions from boundary layer theory.

Finally, on the topic of channel flows of electrically conducting fluid with an imposed magnetic field the author has been involved in numerical studies of transition and turbulence in conducting channel flows with uniform magnetic field. A nonlinear transition mechanism for subcritical Reynolds numbers was investigated for a spanwise magnetic field, and the properties of magnetohydrodynamic turbulence were studied

for both wall-normal and spanwise magnetic field. In addition, the utility of large-eddy simulations with the dynamic Smagorinsky model for such flows was established by direct comparison with direct simulation results.

The summary mostly presents the motivation of the different studies and the essential physics of the systems under consideration. Main results are also described. Details of the mathematical models and numerical methods are given in the publications. The contributions of the author to the individual papers are described in a separate appendix.

2 List of summarized publications

Notice that additional references are listed in a separate appendix.

1. T. Boeck and C. Karcher. Low-Prandtl-number Marangoni convection driven by localized heating on the free surface. *Lect. Notes Phys.*, 628:157–175, 2003.

2. T. Boeck. Bénard-Marangoni convection at large Marangoni numbers: results of numerical simulations. *Adv. Space Res.*, 36(1):4–10, 2005.

3. T. Boeck. Low-Prandtl-number Bénard-Marangoni convection in a vertical magnetic field. *Theoretical and Computational Fluid Dynamics*, 23:509–524, 2009.

4. T. Boeck and A. Thess. Power-law scaling in Bénard-Marangoni convection at large Pandtl numbers. *Phys. Rev. E*, 64:027303, 2001.

5. T. Boeck, A. Nepomnyashchy, and I. Simanovskii. Three-dimensional simulations of water-mercury anticonvection. *Fluid Dynamics and Materials Processing*, 4:11–19, 2008.

6. T. Boeck, A. Nepomnyashchy, I. Simanovskii, A. Golovin, L. Braverman, and A. Thess. Three-dimensional convection in a two-layer system with anomalous thermocapillary effect. *Phys. Fluids*, 14:3899, 2002.

7. T. Boeck and S. Zaleski. Viscous versus inviscid instability of two-phase mixing layers with continuous velocity profile. *Phys. Fluids*, 17:032106, 2005.

8. T. Boeck and S. Zaleski. Instability of two-phase mixing layers: analysis of exact and approximate base flows from boundary layer theory. *J. Noneq. Thermodyn.*, 30(3):215–224, 2005.

9. T. Boeck, P. Yecko, A. Bagué, and S. Zaleski. Instability in two-phase mixing layers. In *Proceedings of the Sixth International Conference on Multiphase Flow*, Leipzig, Germany, 9-13 July 2007.

10. T. Boeck, D. Krasnov, and E. Zienicke. Numerical study of turbulent magnetohydrodynamic channel flow. *J. Fluid Mech.*, 572:179–188, 2007.

11. D. Krasnov, M. Rossi, O. Zikanov, and T. Boeck. Optimal growth and transition to turbulence in channel flow with spanwise magnetic field. *J. Fluid Mech.*, 596:73–101, 2008.

12. D. Krasnov, O. Zikanov, J. Schumacher, and T. Boeck. Magnetohydrodynamic turbulence in a channel with spanwise magnetic field. *Phys. Fluids*, 20:095105, 2008.

13. D. Krasnov, O. Zikanov, J. Schumacher, and T. Boeck. Energy dissipation rates in low-Re_m MHD turbulence with mean shear: Results for channel flow with spanwise field. *Magnetohydrodynamics*, 45(2):155–164, 2009.

14. T. Boeck, D. Krasnov, A. Thess, and O. Zikanov. Large-scale intermittency of liquid-metal channel flow in a magnetic field. *Phys. Rev. Lett.*, 101:244501, 2008.

3 Marangoni and interfacial flows

3.1 Introduction

Flows with free surfaces or interfaces between different fluids are commonplace in nature and technology, and are a major focus of current research. These flows can display interesting phenomena such as topology changes, e.g., when a droplet detaches from a liquid thread. The interplay of surface tension and fluid inertia determines the dynamics in this situation. However, surface tension does not only cause normal forces (Laplace pressure) due to surface curvature. A non-uniform surface tension also causes shear stresses at the interface. This so-called Marangoni effect is an important driving mechanism for interfacial convection. Spatial variations of surface tension can be caused by its dependence on temperature (thermocapillary effect) or concentration (concentration-capillary effect).

Interfacial convection appears in various applications in chemical engineering and materials processing. It can significantly enhance the efficiency of interfacial heat and mass transfer, e.g. in liquid/liquid extraction or gas absorption. It is important in processes involving phase changes, e.g. evaporation from thin films or boiling in heat exchangers [31]. Specifically, thermocapillary convection is responsible for convection in weld pools [36] and in electron beam evaporation of metals for coating purposes [90], where it affects the weld structure and the energetic efficiency. Thermocapillary forces are also a main cause of melt flow in crystal growth [61, 87]. The concentration-capillary effect is used for the drying of silicon wafers in the semiconductor industry [74].

Experimental and theoretical studies of interfacial convection have stimulated and accompanied the development of the theory of pattern formation and nonlinear phenomena in general. The instability in an open layer of fluid heated from below has played a prominent role in this context. It was first studied systematically by Henri Bénard in the early years of the 20th century. He used an open, shallow oil layer and observed the spontaneous appearance of a flow when a certain critical temperature difference was applied. This instability was interpreted and analysed as buoyancy-driven phenomenon by Lord Rayleigh [86]. It was established only in the 1950s by several researchers [18, 83] that the thermocapillary effect can lead to the so-called Bénard-Marangoni instability, which turns out to be the main driving mechanism in the experiments of Bénard. Convection in plane fluid layers with heating from below and free upper surface is therefore known as Bénard-Marangoni convection.

Bénard-Marangoni convection typically displays a regular cellular pattern with a hexagonal structure when the temperature difference is close to the convection threshold. The characteristic cell size is of the order of the layer thickness. However, the Marangoni effect is only dominant for shallow layers. In thicker layers the buoyancy-driven instability identified by Rayleigh contributes as well, and may eventually supersede the thermocapillary mechanism when the liquid layer is sufficiently deep. Another thermocapillary instability mechanism involves surface deformation.

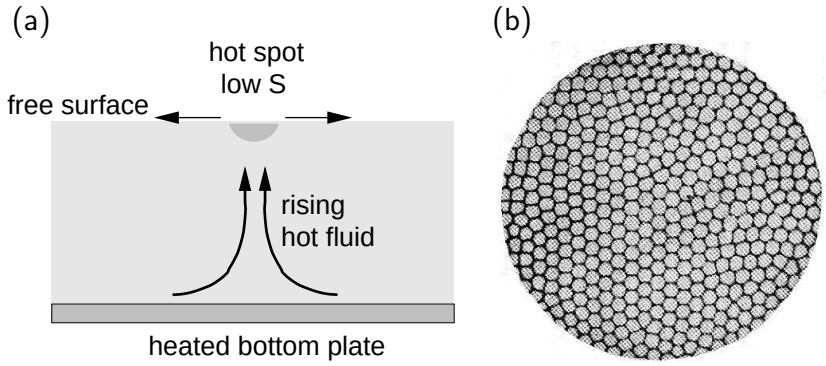

Figure 1: *(a) Instability mechanism in Bénard-Marangoni convection: A localized temperature perturbation at the free surface causes thermocapillary stresses, whereby warm fluid rises towards the surface. (b) Hexagonal cells in Bénard's original experiment. The photograph was reprinted in [28].*

The so-called long-wave instability appears at arbitrarily small temperature difference when the stabilizing effect of gravity is neglected in the stability analysis [93].

Mechanical coupling with the gas phase above the liquid is unessential for the Bénard-Marangoni instability. The flow in the gas phase can be neglected, and the heat conduction in the gas can be approximated by an effective thermal boundary condition at the interface. The mathematical model of Bénard-Marangoni convection is thereby simplified to a single fluid layer.

However, this reduction is inappropriate for interfacial convection between immiscible liquids, where significant mechanical and thermal interactions can occur between the different phases. The simplest configuration is a planar two-layer arrangement, which retains the advantage of a single inhomogeneous direction in space. This is particularly attractive for the study of additional instability mechanisms on account of the presence of an "active" second fluid [78]. The author has explored such instabilities in two different double-layer systems by direct numerical simulations. This work was made in close collaboration with A. Nepomnyashchy and I. Simanovskii. The main interest was on the spatial organisation of the convective pattern, which need not be hexagonal as in the classical Bénard-Marangoni convection.

Further numerical studies by the author have examined the behavior of thermocapillary convection in single layers under strong thermal forcing. These investigations have been motivated in part by scaling analyses of the heat transport in thermocapillary convection with localized heating on the free surface, and by previous numerical simulations of turbulent Bénard-Marangoni convection by the author, which were restricted to two dimensions. The realization of turbulent thermocapillary convection in three-dimensional simulations has therefore been a major objective. The next sections summarize several works on one-layer simulations with strong thermal forcing followed by two numerical works on patterns in two-layer systems.

3.2 Governing equations and numerical methods

The mathematical model of the fluid flow is provided by the incompressible Navier-Stokes equations in combination with the energy equation. Buoyancy effects are treated through the classical Oberbeck-Boussinesq approximation. The system of equations for velocity $\boldsymbol{v}$, pressure p and temperature T is

$$\frac{\partial \boldsymbol{v}}{\partial t} + (\boldsymbol{v} \cdot \nabla)\boldsymbol{v} = -\frac{\nabla p}{\rho} + \nu \nabla^2 \boldsymbol{v} - g\left(1 - \alpha(T - T_0)\right)\boldsymbol{e}_z, \tag{1}$$

$$\nabla \cdot \boldsymbol{v} = 0, \tag{2}$$

$$\frac{\partial T}{\partial t} + (\boldsymbol{v} \cdot \nabla)T = \kappa \nabla^2 T, \tag{3}$$

where the fluid density, kinematic viscosity, thermal expansion coefficient and thermal diffusivity are denoted as ρ, ν, α and κ.

Non-dimensionalisation of these equations leads to two dimensionless parameters. Typically one introduces the Prandtl number

$$Pr = \frac{\nu}{\kappa}, \tag{4}$$

which can be interpreted as the ratio of the timescales of thermal and viscous diffusion. The forcing of the flow by buoyancy is characterized by the Rayleigh number

$$Ra = \frac{\alpha g d^3 \Delta T}{\nu \kappa}, \tag{5}$$

where d is the layer thickness, and ΔT is a characteristic temperature such as the temperature difference across the domain in the case of pure heat conduction. In the case of two fluid layers one has to consider two separate fluid domains with different material properties and separate Rayleigh and Prandtl numbers.

The equations have to be augmented by appropriate boundary conditions on the bounding surfaces of the individual fluid domain. In principle, the shape of the domain is part of the problem because the interface (free surface) may be displaced by the flow. However, one can study many aspects of interfacial convection with the assumption of a static interface[1]. The author has used this approximation in all of his numerical studies of interfacial convection.

[1]The neglect of interface deformation is justified on length scales of order d when the dynamic pressure is small compared with the Laplace pressure of surface deformations with a radius of curvature d. The dynamic pressure may be estimated by the geometric mean of the viscous and thermal velocities ν/d and κ/d, whereby one arrives at the crispation number $Cr = \rho\nu\kappa/Sd$. A large surface tension S - quantified by the condition $Cr \ll 1$ - allows one to make use of the static interface assumption on lateral scales comparable with d. The advantage of this assumption for numerical simulations quite significant: One has effectively to deal with single-phase flows on fixed computational domains in this case. When the interface geometry is part of the problem, the simulations require a completely different approach with moving grids or fixed-grid methods with variable fluid properties. Numerical methods for such general two-phase flows still have considerable problems and limitations in terms of reliability and accuracy, and it is therefore advantageous to employ proven and computationally efficient methods for single-phase flows where possible.

The assumption of a static planar interface eliminates the need to consider the balance of normal forces on the interface, which is chosen as $z = const$. The balance of tangential forces is given by the conditions

$$\rho_1\nu_1\frac{\partial u_1}{\partial z} - \rho_2\nu_2\frac{\partial u_2}{\partial z} = -\frac{\partial S}{\partial x}, \tag{6}$$

$$\rho_1\nu_1\frac{\partial v_1}{\partial z} - \rho_2\nu_2\frac{\partial v_2}{\partial z} = -\frac{\partial S}{\partial y}, \tag{7}$$

on the horizontal velocities u and v, where the index 1 refers to the top and index 2 to the bottom layer [63, sec. 61]. The temperature dependence of surface tension is usually approximated by a linear relation

$$S = S_0 - \gamma(T - T_0). \tag{8}$$

Nondimensionalisation of the tangential force conditions with this relation gives rise to the so-called Marangoni number

$$Ma = \frac{\gamma d\Delta T}{\rho\nu\kappa}, \tag{9}$$

where d and the quantities in the denominator could be that of the top or bottom layer or any dimensionally matching combination of the fluid properties. The Marangoni number describes the forcing of the flow by the thermocapillary effect. In the single layer approach one simply neglects the shear stresses by the top layer in eq. (6,7).

The numerical simulations of interfacial convection in a single or two coupled, plane layers have been performed with pseudo-spectral methods based on Fourier-Chebyshev modal expansions of the hydrodynamic fields. The velocity is represented through a velocity potential formulation known as poloidal-toroidal representation, whereby the incompressibility constraint is satisfied automatically. The methods have been implemented by the author for distributed memory parallel computers using domain decomposition on the array of spectral expansion coefficients. The single-layer code is described in detail in the doctoral thesis of the author [19], and the extension to the two-layer problem in the publications [6, 24].

3.3 One-layer systems

3.3.1 Three-dimensional simulations [1, 2]

Low Prandtl numbers are typical of liquid metals and semiconductors, which have high thermal conductivity. Investigations of the flow structure and heat transport in thermocapillary flows of such liquids are of interest for materials processing, and for the understanding of fluid turbulence near free boundaries.

The author had previously studied Marangoni convection at low Prandtl numbers in his doctoral thesis and observed clear power-law scaling of the Nusselt and

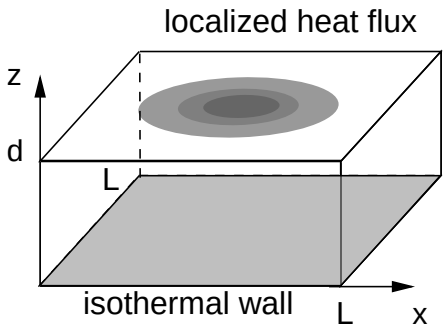

Figure 2: *Computational domain and the thermal boundary conditions for the study of Marangoni convection with heating from above.*

Reynolds numbers in two-dimensional simulations of the Bénard-Maragoni system. At that time, three-dimensional simulations could not be realized for sufficiently large Marangoni numbers because of limited computer resources. The publications [1, 2] present such three-dimensional simulations with $Pr = 0.1$ for two different configurations. The first is the Bénard-Marangoni system with uniform heating from below, which has been studied with periodic boundary conditions in the two horizontal directions (x, y). The second configuration has non-uniform heating from above and lateral confinement by adiabatic, free-slip walls. It corresponds reasonably well to the theoretical model formulated by Pumir and Blumenfeld [84] for the heat transport in electron beam evaporation, which provides scaling laws for the characteristic velocity and temperature with the heat flux. The chosen lateral boundary conditions in the second configuration are without alternative because of the use of the Fourier system in the modal expansion of the hydrodynamic fields.

The results for localized heating from above (Fig. 2) are described in the publication [1] and will be summarized first. The aspect ratio of the square box is $L/d = 2$ and the heat flux distribution at the free surface is prescribed as a centered Gaussian of the form

$$q(x, y) = q_{\max} \exp\left(-5\,\frac{(x-d)^2 + (y-d)^2}{d^2}\right). \tag{10}$$

This heat flux distribution is compatible with the reflection and rotation symmetries of the computational domain[2]. The temperature scale Θ and the Marangoni number are defined as

$$\Theta = \frac{q_{\max} d}{\lambda}, \qquad Ma = \frac{\gamma q_{\max} d^2}{\rho \lambda \nu^2}, \tag{11}$$

where λ denotes the thermal conductivity. The Prandtl number is $Pr = 0.1$. Buoyancy effects are neglected ($Ra = 0$).

The state of pure heat conduction has a non-uniform temperature distribution on the free surface because of the non-uniform heating. It is illustrated in Fig. 3(a) and

[2]Eq. (23) for the heat flux distribution in [1] is incorrect.

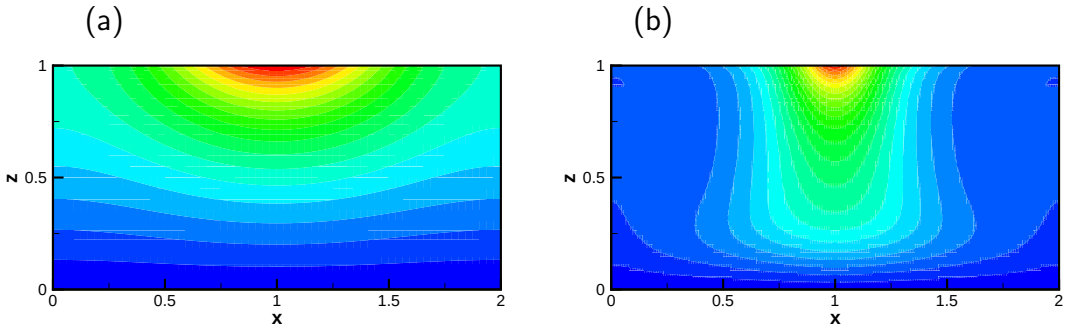

Figure 3: *Temperature distributions in the vertical midplane for Marangoni convection with heating from above: (a) corresponds to the conductive state* $Ma = 0$*; (b) shows a snapshot at some point during the oscillation period at* $Ma = 1.4 \times 10^5$.

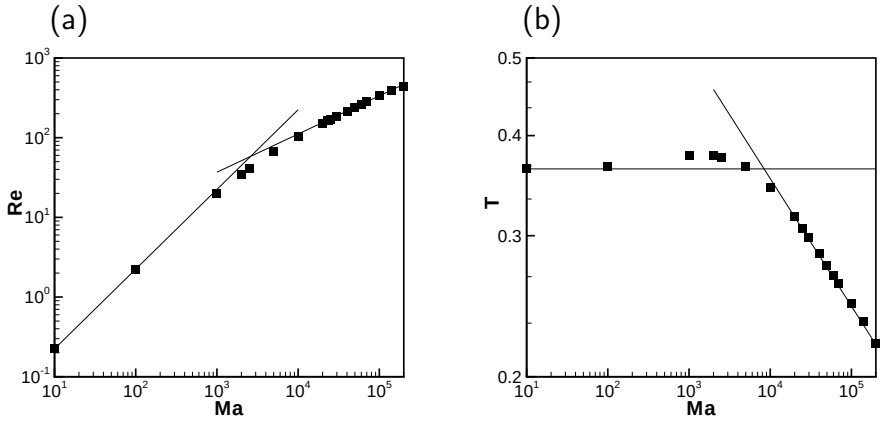

Figure 4: *Dependence of Reynolds number (a) and average temperature (b) on* Ma *for Marangoni convection with heating from above.*

causes appearance of Marangoni convection as soon as $Ma > 0$. The laminar flow at small Ma resembles a deformed toroid with upflow in the middle of the box and downflow at the lateral walls. This global flow pattern persists at higher Ma even after the onset of time dependence and chaotic flow. The increasing loss of symmetry with increasing Ma is documented in the publication [1].

The transformation of the temperature distribution by the flow is illustrated by vertical temperature profiles in the plane $y = L/2$ shown in Fig. 3(b). In contrast to the conductive state in Fig. 3(a), the isotherms are concentrated below the heat source in Fig. 3(b), and the temperature variation in the outer regions near the walls is minimal. This structure of the isotherms is caused by the strong vortical motion near the walls. The temperature distribution on the free surface is also modified considerably, and does no longer show the concentric arrangement of the conductive state. Nevertheless, the highest instantaneous temperature is located at the center of

the free surface for all values of Ma realized in the simulations except for the highest $Ma = 2 \times 10^5$. At this value of Ma the flow becomes chaotic and loses its spatial symmetry.

The rms velocity (Reynolds number) and the time-averaged temperature at the center of the free surface are shown in Fig. 4 as functions of Ma. One can clearly identify two distinct scalings. For low Ma, the two quantities scale as

$$Re \sim Ma^1, \quad T \sim Ma^0. \tag{12}$$

These relations correspond to laminar flow at moderate Reynolds and low Peclet number, i.e. there are no boundary layers and the temperature distribution remains close to the conductive state. For $Ma \gtrsim 10^4$ the Peclet number remains no longer small, and the temperature is reduced in comparison with the conductive state by the additional convective heat transfer. The relations

$$Re \sim Ma^{0.48}, \quad T \sim Ma^{-0.16}. \tag{13}$$

are obtained from best fits to the data between $Ma = 5 \times 10^4$ and $Ma = 1.4 \times 10^5$. This scaling is in fair agreement with the model by Pumir and Blumenfeld, which predicts exponents $1/2$ for Re and $-1/4$ for T in case of laminar boundary layer flow [84]. The turbulent regime is also modeled by these authors, but the simulations could only realize a weakly turbulent state at the highest value $Ma = 2 \times 10^5$. The discrepancy between the boundary layer model and simulation in the scaling exponents for T is not particularly surprising since the model assumes homogeneous temperature except for a hot spot beneath the surface. This assumption is not fully adequate for the temperature distribution in Fig. 3(b).

Simulation results for the Bénard-Marangoni system with the Prandtl number $Pr = 0.1$ are documented in the publication [2]. In this configuration, the heat is transported from the isothermal bottom to the free surface, where a uniform heat flux density q is assumed. The temperature scale Θ and the Marangoni number are defined as

$$\Theta = \frac{qd}{\lambda}, \quad Ma = \frac{\gamma q d^2}{\rho \lambda \nu \kappa}. \tag{14}$$

Buoyancy effects are neglected ($Ra = 0$). The horizontal directions are periodic with dimensions $L_x = L_y = 2\pi d$.

In contrast to the previous case with heating from above, convection can only be sustained for $Ma \gtrsim 80$ because of the finite instability threshold. The flow pattern at this threshold consists of stationary hexagonal cells with downflow in the cell center [96]. For higher Ma these so-called inverted hexagonal cells are unstable and the flow aquires time-dependence and spatial irregularity. In the parameter range $Ma \geq 500$ considered in [2] the flows appear to be turbulent. Fig. 5(a,b) show a snapshot of the surface temperature distribution and mean temperature profiles. The temperature difference is reduced by increasing Ma because of the additional convective heat transport.

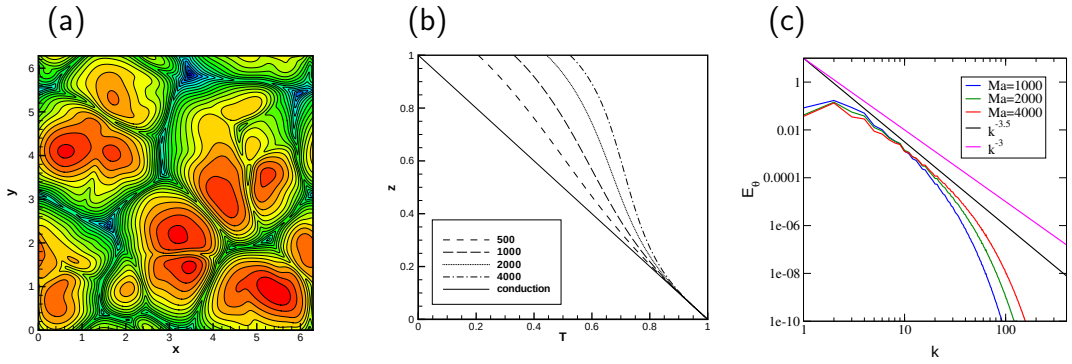

Figure 5: *Bénard-Marangoni convection at $Pr = 0.1$: (a) snapshot of surface temperature at $Ma = 4000$, (b) mean vertical temperature profiles, (c) surface temperature spectra for several Ma. The power laws in (c) are shown for comparison.*

For the interval $500 \leq Ma \leq 4000$ covered in the three-dimensional simulations, the Reynolds number Re and mean temperature difference can be described by power laws in Ma with exponents that are fairly close to those from two-dimensional simulations of turbulent Bénard-Marangoni convection at the same Prandtl number [22]. These exponents are also in reasonable agreement with a simple model from [22] based on laminar thermal boundary layers in combination with a turbulent estimate $\varepsilon \sim Re^3$ for the viscous dissipation rate ε. However, at the same Re the viscous dissipation rate ε is considerably larger in the three-dimensional case than in the two-dimensional case considered in [22].

Another similarity with the two-dimensional results concerns the temperature distribution on the free surface. Fig. 5(a) shows that there are relatively large, warm patches (in red) with upflow and small gradients, whereas the cold downflow regions are narrow bands (in blue) with a high density of isotherms. This structure is reflected in the surface temperature spectra $E_\theta(k)$ shown in 5(c), which are calculated from the Fourier coefficients $\hat{\theta}_{\boldsymbol{k}}$ with wavevector $\boldsymbol{k}$ by

$$E_\theta(k) = \sum_{k-\Delta k<|\boldsymbol{k}|<k+\Delta k} |\hat{\theta}_{\boldsymbol{k}}|^2. \tag{15}$$

The wavenumber increment $\Delta k = \pi/L_x$ is prescribed by the periodicity length of the computational domain. Time-averaged spectra display an approximate k^{-4} decay with the wavenumber k. This power law is characteristic of discontinuities in the gradients, which are localized along lines. It has been originally suggested by Saffmann for the distribution of vorticity in two-dimensional turbulence [88]. The k^{-4} decay is different from Bénard-Marangoni convection at large Prandtl numbers, where an approximate k^{-3} spectrum has been found in numerical simulations [98]. The smaller exponent -3 points to stronger singular structures, namely point singularities in the Laplacian of the surface temperature [98].

3.3.2 Two-dimensional simulations [3, 4]

The comparison between two- and three-dimensional results for Bénard-Marangoni convection at low Prandtl number in the publication [2] shows that that two-dimensional, laminar convection provides the most efficient heat transfer. This so-called inertial convection occurs for two-dimensional roll cells with a near inviscid balance of pressure gradients and nonlinear terms in the Navier-Stokes equations. For Bénard-Marangoni convection, this mode of convection has been realized in two-dimensional numerical simulations by using the free-slip condition at the bottom of the fluid layer [21]. Inertial Bénard-Marangoni convection provides a characteristic scaling

$$Nu = \frac{\Delta T_0}{\Delta T} \sim Ma^{1/3} \tag{16}$$

of the Nusselt number Nu, which is independent of the Prandtl number. In eq. (16), the quantity ΔT denotes the average temperature difference across the layer. Convection reduces ΔT in comparison with ΔT_0 in the conductive state since the heat flux is prescribed. The ratio $\Delta T_0/\Delta T$ is therefore an appropriate measure of the heat transfer by convection. The Marangoni number in eq. (16) is defined by eq. (9).

The remarkable properties of inertial convection provided the motivation for two subsequent studies of two-dimensional Bénard-Marangoni convection. In the first study, the effect of a vertical magnetic field on Bénard-Marangoni convection at low Prandtl number is considered. The results are described in the publication [3], which also includes some three-dimensional simulations. The second study [4] considers the opposite case of two-dimensional Bénard-Marangoni convection at very large Prandtl numbers. Two-dimensional simulations allow one to reach much larger Marangoni numbers than three-dimensional ones because the computational effort at the same Marangoni number is considerably smaller.

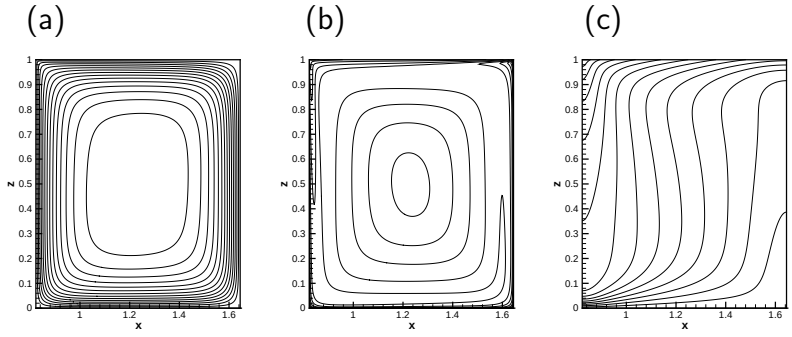

Figure 6: *Isocontours of (a) streamfunction ψ, (b) vorticity ω and (c) temperature for steady two-dimensional Bénard-Marangoni convection with $Ha = 20$, $Ma = 32000$, $Pr = 0.02$, $L_x = 2\pi/3.82$. Only a single roll is shown due to the imposed mirror symmetry. The flow orientation is counter-clockwise.*

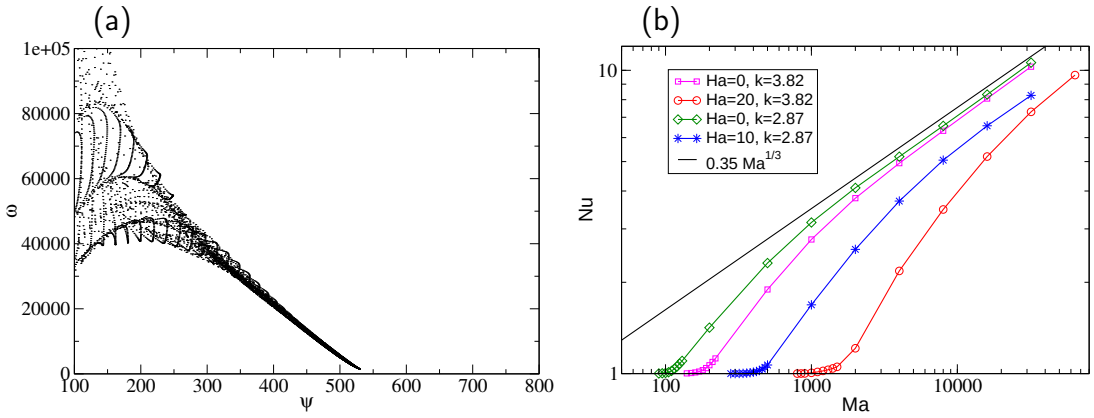

Figure 7: *Two-dimensional Bénard-Marangoni convection with vertical magnetic field and* $Pr = 0.02$*: (a) scatter plot of* ω *and* ψ *for* $Ha = 20$*,* $Ma = 64000$*,* $Pr = 0.02$*,* $L_x = 2\pi/3.82$*; (b)* $Nu(Ma)$ *for different domain sizes* $L_x = 2\pi/k$ *and Hartmann numbers.*

A vertical magnetic field raises the threshold for the Bénard-Marangoni instability and modifies the unstable wavelength [106, 97]. However, the magnetic damping of the flow by the Lorentz force is linear in the velocity[3], and should therefore not preclude the possibility of a near inviscid balance when the flow is sufficiently fast. The simulations in paper [3] are in line with this expectation. Fig. 6 shows isolines of streamfunction and vorticity as well as isotherms for a magnetic induction B corresponding to the Hartmann number $Ha = 20$. The symmetric form and the visual resemblance of isolines of streamfunction and vorticity in Fig. 6(a,b) are indications of a near balance of nonlinear and pressure terms in the Navier-Stokes equations. This is confirmed by the scatter plot of streamfunction ψ and vorticity ω for a single roll in Fig. 7(a). It reveals a functional relation $\omega(\psi)$ for large ψ, which is approximately linear. Such values of ψ correspond to the core region of the convection roll. The functional relation between ψ and ω disappears towards the boundary layers, where viscosity becomes important. The finite slope in the $\omega(\psi)$ relation is an indication of the Joule dissipation. It is absent in the non-magnetic simulations, where the vorticity is constant by the Prandtl-Batchelor theorem [35, sec. 3.5]. The paper [3] considers this aspect in more detail.

The effect of the magnetic field on the Nusselt number is shown in Fig. 7(b). The curves for different parameter combinations (two domain sizes $L_x = 2\pi/k$ and two Hartmann numbers) demonstrate the shift in the instability threshold to higher Ma by the magnetic damping. In contrast to the two cases with $Ha = 0$, there is no clear indication of the scaling (16) for Nu with Ma for $Ha > 0$. This is not surprising since the temperature field still lacks the isothermal core in the bulk in Fig.

[3]Section 5.2 describes the mathematical model for conducting flows. The Hartmann number is defined in eq. (42).

6(c), which is assumed for the scaling relation (16). This observation applies for all simulations with magnetic field performed for paper [3]. Eq. (16) may nonetheless become valid at even larger Marangoni numbers.

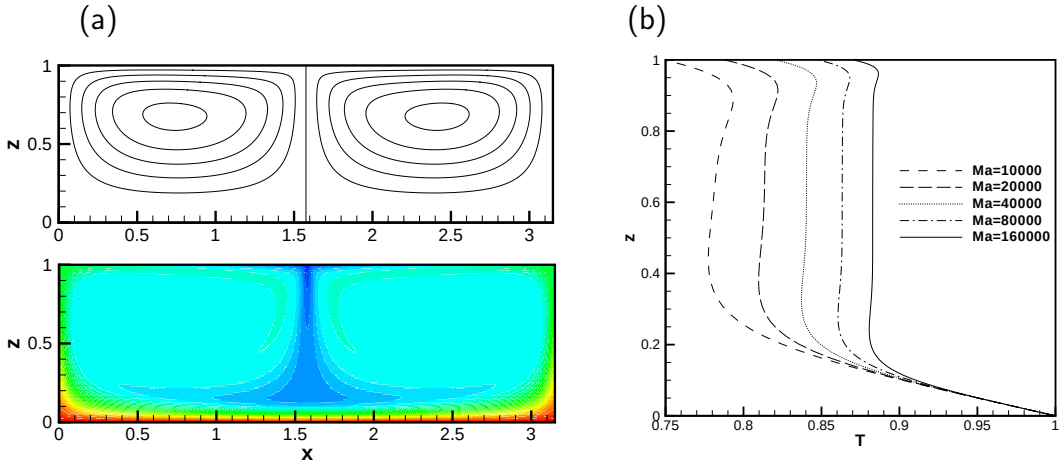

Figure 8: *Two-dimensional Bénard-Marangoni convection with infinite Pr: (a) streamfunction (top) and temperature (bottom) for $Ma = 320000$; (b) mean temperature profiles for different Ma. The thermal boundary layer at the bottom is considerably thicker than at the free surface.*

Bénard-Marangoni convection at large Prandtl numbers is dominated by viscosity. Any viscous boundary layers will therefore be considerably wider than thermal boundary layers. The limit of infinite Prandtl number eliminates inertia completely, and the velocity field then lacks any boundary layers. Thermal boundary layers can nonetheless develop in this case, which is explored in paper [4]. The two-dimensional simulations at infinite Prandtl number from paper [4] do not provide time-dependent solutions, i.e. the flow organizes in stationary roll cells. The significant advection of the temperature field leads again to approximately isothermal core regions, which can be seen in Fig. 8(a). However, the mechanical boundary conditions at the bottom play an important role for the heat transport in this case. For free-slip conditions, the velocity is finite at the lower wall, and the thermal boundary layer has therefore a characteristic thickness of order $V^{-1/2}$, where V is the spatial rms velocity. The thermal boundary layer at the free surface has the same property, and one obtains a Nusselt number scaling with $Ma^{1/3}$ as in eq. (16) for inertial convection.

However, the boundary layer scaling changes when the no-slip condition is used at the bottom wall. In this case, the velocity is approximately proportional to the distance from the bottom wall, and the thermal boundary layer has then a characteristic thickness of order $V^{-1/3}$, where V is again the integral velocity scale. This estimate can be found in [92]. The different behavior of the thermal boundary layers at the bottom wall and at the free surface is apparent from Fig. 8(b). As a consequence, the lower boundary layer limits the heat transport in this situation. The asymptotic

model for the Nusselt number scaling is thereby modified, and provides

$$Nu \sim Ma^{2/9}. \tag{17}$$

The numerical results in [4] agree closely with the relation (17).

3.4 Two-layer systems

Two-layer systems are interesting because the mechanical and thermal interactions between immiscible liquids can introduce instability mechanisms that are qualitatively different from those in the one-layer approximation. The author has studied such instabilities in two different two-layer systems mainly in collaboration with A. Nepomnyashchy and I. Simanovskii. The two studies have been published in the papers [5, 6]. In contrast to the one-layer approximation, specific substances had to be chosen because of the large parameter space associated with the material properties of the fluids.[4]

3.4.1 Anticonvection [5]

The study is concerned with the so-called anticonvection, i.e. buoyancy-driven instability with uniform heating from above. The liquids are mercury and water as suggested by Welander, who noted that anticonvection can exist in a two-layer system when the thermophysical properties of the liquids are very different [105]. A suitable configuration for anticonvection requires a lower, dense liquid of high thermal conductivity combined with an upper liquid with considerably smaller heat conductivity. The instability mechanism can then be described by considering a rising fluid element in the lower layer approaching the interface. Because of continuity and mechanical coupling at the interface, a corresponding downward motion is generated in the upper liquid. This downward motion in the top layer carries warmer fluid towards the interface, whereby the temperature rises in the lower layer near the interface thanks to the high thermal conductivity of the lower liquid. This way, the rising fluid element in the lower layer can obtain an excess temperature relative to the mean (positive) temperature gradient and thereby sustain its motion through positive buoyancy. In the top layer, the downward flow is opposed to the buoyancy forces.

The simulations in paper [5] were performed for equal thicknesses $d_1 = d_2$ of mercury and water. The control parameter is the Grashof number

$$G = \frac{\alpha_1 g |\Delta T| d_1^3}{\nu_1^2} \tag{18}$$

defined with the material properties and the thickness d_1 of the water layer. The temperature difference ΔT is the total applied temperature difference across both

[4] Six independent, dimensionless quantities are necessary to characterize the system, e.g., the ratios of densities, viscosities, thermal conductivities, thermal diffusivities, expansion coefficients, and one of the two Prandtl numbers.

liquid layers. The absolute value of ΔT is used for convenience in eq. (18) since ΔT is negative for heating from above. Linear stability analysis provides a critical value $G_c \approx 2010$ for this configuration with a critical wavenumber $k_c d_1 \approx 0.97$.

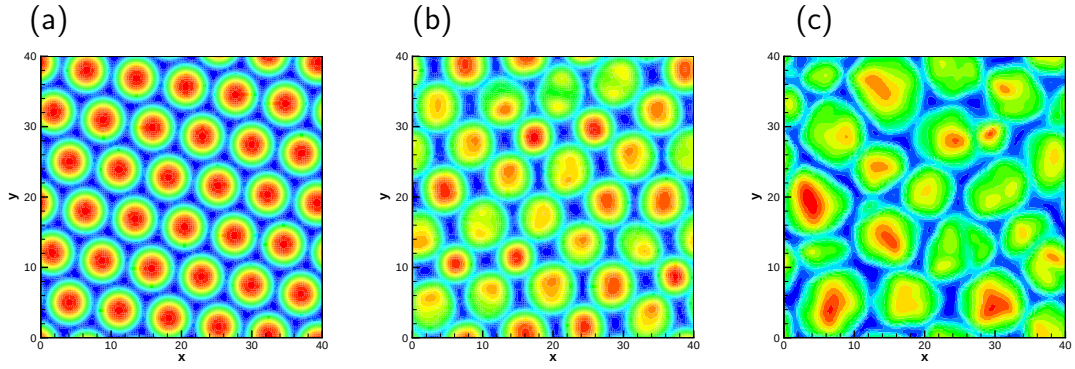

Figure 9: *Interface temperature snapshots for anticonvection at (a) G=2050, (b) G=3150, (c) G=5000. The aspect ratio is* $L_x = L_y = 40 d_1$.

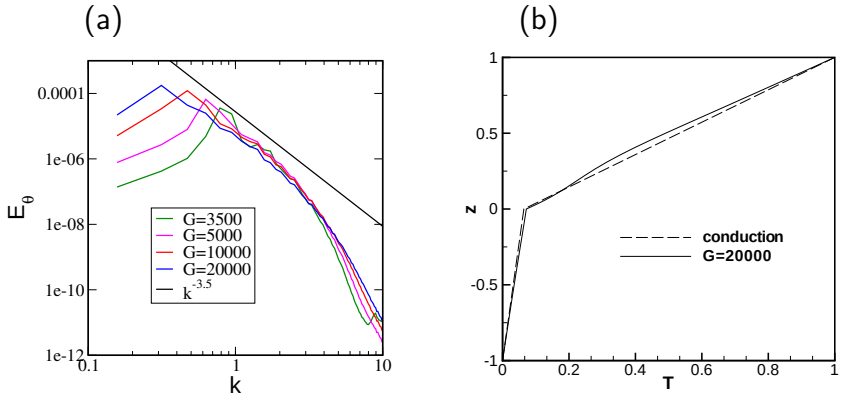

Figure 10: *Anticonvection: (a) surface temperature spectra for several* G*, (b) mean temperature profile.*

The convective pattern on the interface is shown in Fig. 9 for different values of G. Near the threshold G_c the pattern is composed of hexagonal cells and free of defects (Fig. 9(a)). The orientation of the flow in the center of a cell is upwards in the lower mercury layer. This hexagonal pattern can be sustained for $G < G_c$ down to about $G_{\min} \approx 1730$. This subcritical interval $(G_c - G_{\min})/G_c \approx 0.14$ is considerably larger than the interval $(Ma_c - Ma_{\min})/Ma_c \approx 0.01$ in one-layer Bénard-Marangoni convection at small or large Prandtl numbers [23, 98]. The flow becomes time-dependent around $G \approx 3000$, and develops an approximately rhombic cellular pattern around $G \approx 3200$. This pattern is not stable, and becomes more and more disordered as G is increased to $G = 5000$ and beyond. At the same time, the cellular structures

grow in size. This trend is apparent from Fig. 9, but it can be quantified further by time-averaged spectra E_θ of the temperature on the interface (Fig.10a) . They are calculated by eq. (15). The peak of E_θ is around $k \approx 1$ for $G = 3500$ and shifts to smaller values upon increasing G. For $G = 20000$, the decaying part of the spectrum can be approximated by a $k^{-3.5}$ power law for wavenumbers from the peak up to about $k \approx 3$, i.e., over about one decade in k. This behavior is similar to that of single-layer Bénard-Marangoni convection at $Pr = 0.1$ considered in the previous section.

Due to the peculiar nature of the instability mechanism it cannot be expected to enhance the heat transfer across the two liquid layers. This was already noted by Welander, who pointed out that measurements of the integral heat flux as a function of temperature difference can probably not reliably detect anticonvection in an experiment. This conclusion applies even for $G = 20000$. It can be seen in Fig. 10(b) that the temperature drop across the mercury is fairly small, and that the mean temperature profile differs only slightly from the conductive profile.

3.4.2 Convection with anomalous thermocapillary effect [6]

The second study has been made for a system where the two liquids have fairly similar thermophysical properties. The upper layer is a silicone oil (10 cS viscosity) and the lower layer is ethylene glycol. In contrast to the anticonvection problem described above, the layers are heated from below, and Marangoni forces are taken into account. However, the interfacial tension for this liquid-liquid system increases with temperature for temperatures somewhat above room level. This behavior is referred to as anomalous thermocapillary effect. For other liquid-liquid systems, the interfacial tension usually decreases with temperature.

The mechanical coupling on the interface by the shear stresses implies that the buoyancy instability mechanism in one layer is opposed by that of the other layer. When the buoyancy mechanism in the lower layer dominates, then the normal thermocapillary effect adds to the forcing, and supports the instability. The situation is reversed when the buoyancy mechanism dominates in the upper layer. In this case, buoyancy and thermocapillary forces oppose each other, and can give rise to linear oscillatory instability. The same argument can be made for the anomalous thermocapillary effect when the roles of upper and lower layer are reversed. Competition of buoyancy and thermocapillary forces can lead to oscillatory instability when buoyancy in the lower layer dominates. For this reason, both stationary and oscillatory instability is expected to occur in the 10 cS silicone oil/ethylene glycol system. The patterns associated with the oscillatory instability are the main interest in [6].

In addition to the six dimensionless quantities for the material properties, the two-layer system is characterized by the ratio d_1/d_2 of the layer thicknesses, and Grashof and Marangoni numbers

$$G = \frac{\alpha_1 g \Delta T d_1^3}{\nu_1^2}, \quad M = \frac{\gamma \Delta T d_1}{\rho_1 \nu_1 \kappa_1} \tag{19}$$

for the buoyancy and Marangoni forces. The ratio $d_1/d_2 = 5/9$ of layer thicknesses is adopted in [6] since a previous linear stability analysis had provided both stationary and oscillatory instability for this choice of d_1/d_2 [26]. The corresponding stability diagram is shown in Fig. 11. The Marangoni number is negative because the temperature coefficient γ in eq. (8) is negative for the anomalous thermocapillary effect.

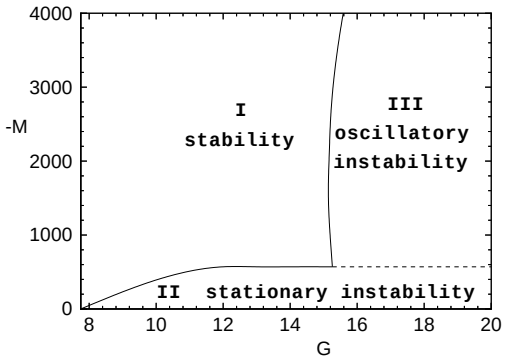

Figure 11: *Linear stability results for two-layer convection with anomalous thermocapillary effect and* $d_1/d_2 = 5/9$.

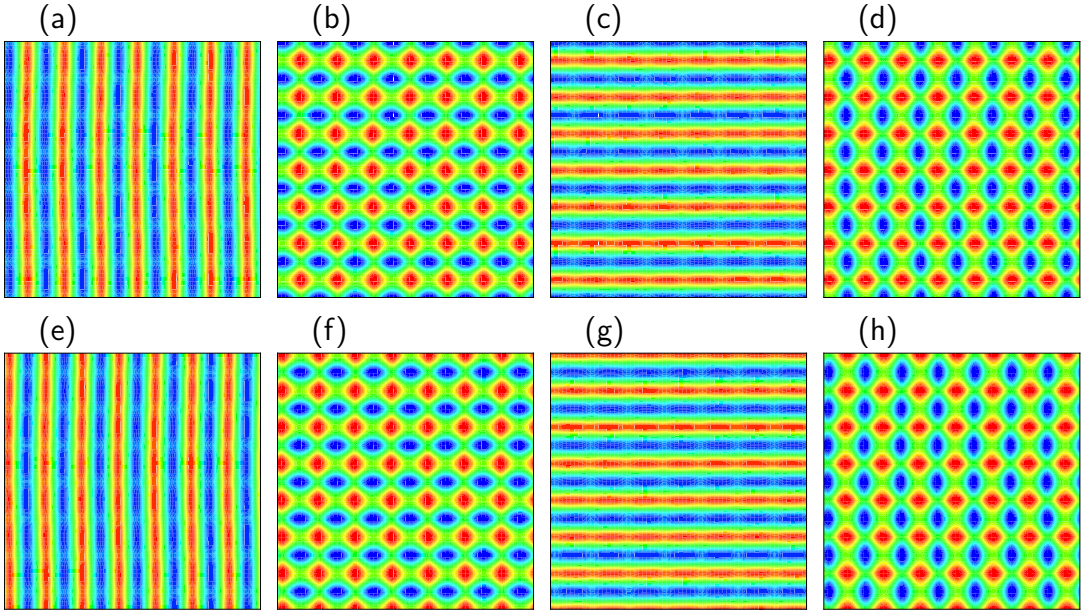

Figure 12: *Snapshots of the interfacial temperature during one oscillation period of alternating rolls for* $G = 20$, $M = -1000$.

The numerical simulations in the paper [6] have explored the different instability regions in Fig. 11. The parameters were restricted to $G < 20$ and $M > -4000$. In

the region II of stationary instability the convection appears in the form of parallel rolls when $|M|$ is small and as hexagonal cells for larger $|M|$. In the terminology of pattern formation theory, these pattern are "one-wave" and "three-wave" patterns because hexagons can be described as a superposition of three plane waves $\exp(i\boldsymbol{k}_m \cdot \boldsymbol{x})$ with wave vectors $\boldsymbol{k}_m$ of equal magnitude but different orientation in the (x, y)-plane. The appearance of hexagons is expected for flows with thermocapillary forcing, whereas rolls are typical for predominantly buoyancy-driven flow.

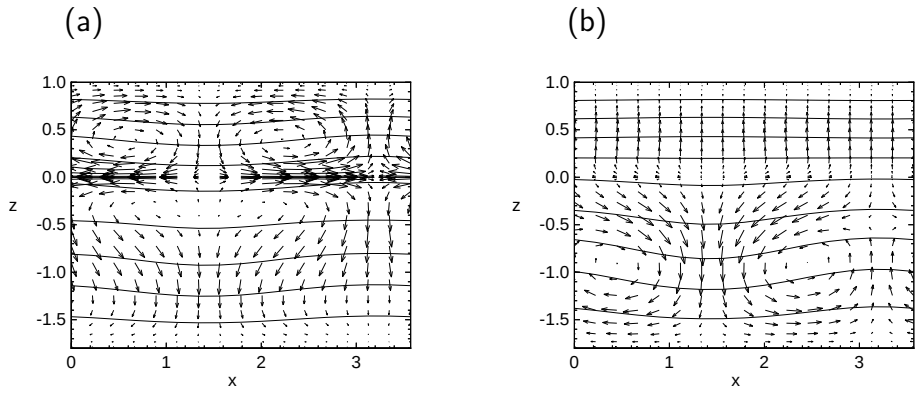

Figure 13: *Vertical structure of velocity field and isotherms of a single pair of alternating rolls for $G = 15.5$ and $M = -1000$: Snapshots taken when the flow is approximately two-dimensional in the top layer. (a) Top layer flow in the (x, z)-plane and (b) top layer flow perpendicular to the (x, z)-plane. The interface is located at $z = 0$.*

For the oscillatory instability there are numerous conceivable periodic patterns near the onset of convection. They have been theoretically classified for square and hexagonal lattices, i.e. for underlying "two-wave" and "three-wave" configurations with wave vectors forming right angles and $2\pi/3$ angles, respectively [30]. In the simulations, it turns out that the typical flows in region III are alternating rolls, which belong to the "two-wave" variety. Other possible solutions with the same underlying spatial symmetry would be traveling or standing rolls and traveling or standing squares. The time evolution of alternating rolls is illustrated by snapshots of the interfacial temperature in Fig. 12. One observes a roll pattern that changes its orientation periodically. In addition, it is shifted by a half-period in space after the first change of orientation. A typical vertical structure of the velocity field for alternating rolls is illustrated in Fig. 13 at two different times. The z-dependent phase of the oscillatory mode prevents it from becoming two-dimensional at any point during the cycle.

Particularly interesting flows can be found near the boundary between stationary and oscillatory instability, i.e. regions II and III in Fig. 11. The preferred pattern in region II is a "three-wave" pattern (hexagons), whereas it is a "two-wave" pattern in region III (alternating rolls). The simulations show that the "three-wave" flows become time-dependent as one approaches the boundary from within region II before

the "two-wave" type emerges. Moreover, these flows typically have spatial defects or modulations and may evolve chaotically. They can therefore no longer be described in the framework of bifurcation theory for spatially periodic patterns.

3.5 Summary

Marangoni convection with strong thermal forcing at low Prandtl number is an important aspect of several technological applications, e.g. welding and crystal growth. Numerical simulations are a useful tool for the understanding of such flows, which are difficult to study in controlled experiments. From the application viewpoint it is desirable to include as much realism as possible in the numerical models. However, from a fundamental perspective it is preferable to study simple configurations in detail before turning to complex models. The latter approach is followed in the works [1, 2, 3, 4] for one-layer convection, which focus on the heat transport and the structure of the hydrodynamic fields. The present understanding of these aspects of strongly nonlinear Marangoni convection is fairly limited.

The three-dimensional simulations with heating from above [1] have shown that laminar boundary layer flow postulated in [84] can be realized and exhibits the theoretically predicted scaling. The turbulent parameter range could barely be reached in [1]. The flow turns out to be fairly stable due to the constraining lateral boundaries. For the Bénard-Marangoni system in [2] the cellular structures are not stabilized by lateral walls, and the flow becomes spatially disordered and turbulent at fairly low Marangoni number. A detailed analysis of the turbulence properties has not been made in [2]. It will be the subject of future work. To the knowledge of the author, the publication [3] presents the first computational study of nonlinear Bénard-Marangoni convection with a magnetic field.

The two-dimensional simulations in [4] are useful because they allow one to reach very large Ma. The laminar flows at large Ma provide benchmarks for the three-dimensional case and for upper-bound theories of heat transport in Bénard-Marangoni convection, which have presently only considered the case $Pr \to \infty$ [37]. They are also interesting for simplified, semi-analytic descriptions such as those developed for Rayleigh-Bénard convection at large Prandtl number [29].

Two-layer systems have been extensively studied in two-dimensional simulations [78]. The publications [5, 6] are among the first nonlinear studies in three dimensions. At the instability thresholds one finds regular patterns that are known from other systems. The destabilization and transformation of these patterns for stronger forcing is discussed in [5, 6], and should be interesting for theoretical modeling of patterns, and for possible experimental studies. Anticonvection has so far not been realized in experiments.

4 Instability of two-phase shear layers

4.1 Introduction

The breakup of a continuous mass of liquid into droplets is of considerable importance in nature as well as in technological applications. The first investigations date back to Savart in the early 19th century. Plateau identified the static instability of a cylindrical liquid column under surface tension in 1849 using an energy minimization argument. Dynamical effects in this process were taken into account about 30 years later by Lord Rayleigh [28, 38]. A detailed review of such surface-tension-driven instabilities is given by Eggers [39].

In many applications liquid fragmentation (atomization) is not driven by surface tension but by shear forces. The typical configurations are the injection of a fast liquid jet or sheet into a stagnant or slowly moving gas phase [69], or the acceleration of a slowly moving liquid by a surrounding gas stream of high velocity. Such rapid atomization of liquids is important for achieving high combustion rates in furnaces and thermal engines, or for efficient spray deposition or spray cooling processes in the metal processing industry, the food industry, chemical engineering and agriculture [66]. In nature, sea spray is important for the heat and mass exchange between atmosphere and ocean.

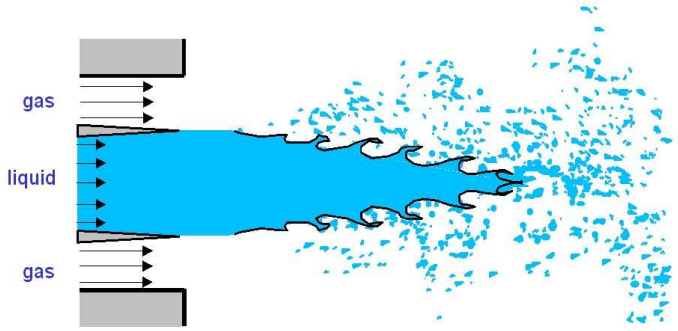

Figure 14: *Schematic representation of atomization from a concentric nozzle by a fast gas stream.*

The atomization of a liquid under the influence of a fast gas stream is a complex process, which is initiated at the nozzle exit. It is shown schematically in Fig. 14 for atomization from a concentric nozzle. The fast gas stream surrounds the liquid jet, which is discharged with a relatively low velocity. The high velocity difference between gas and liquid causes high shear at the interface and thereby supports the Kelvin-Helmholtz instability. The interface develops a wavy deformation that grows with the distance from the nozzle exit. This interface deformation can be characterized

by an interval of wavelengths with certain velocities and amplification rates. At larger downstream distances transverse perturbations develop on the crests of the propagating waves, which are drawn into ligaments by the gas stream. The stretching of the ligaments eventually leads to the detachment of droplets at their tips. The detachment of liquid from the jet or sheet characterizes the so-called primary phase of atomization. The secondary phase is characterized by further destabilization and fragmentation as well as collision and merging of the detached liquid in the gas stream due to aerodynamic forces [64, 73].

The quantitative description of atomization as an inhomogeneous turbulent two-phase flow presents numerous challenges for theory and experiment. Typical mean features of the flow accessible for experimental measurement are the length of the liquid core before it is completely broken up by primary atomization, and the opening angle of the spray [64]. On the statistical side the main interest is in the size distribution of the droplets emerging from the secondary phase of atomization. Moreover, the development of the initial deformation of the liquid interface can also be observed in experiments [73, 85].

Theoretical understanding of atomization remains fairly limited, especially with regard to the complex nonlinear dynamics of the interface in the primary phase and the subsequent processes in the secondary phase. The existing models for features such as the length of the liquid core or the droplet size statistics involve significant simplifications and assumptions of uncertain validity [64]. Detailed numerical simulations of atomization are therefore highly desirable not only from an engineering perspective but also for progress on the theoretical side. The development of numerical methods for this purpose is an active field of research. State-of-the-art simulations can already reproduce major qualitative features of atomization, although they fall short of realistic physical parameters found in experiments and actual applications [42]. The post-processing of such simulations also poses some additional challenges such as the extraction of droplet size statistics or similar quantities.

As mentioned earlier, the prerequisites for Kelvin-Helmholtz instability exist near the nozzle due to the strong shear near the undeformed interface. It is therefore a common view that the initial stage of the evolution from separate streams to turbulent flow with dispersed liquid is controlled by this instability, and that its characteristic features (lengthscales, rates of growth and wave speeds) correspond to those of the most amplified linear perturbations. The prediction of these properties should therefore be feasible in the framework of hydrodynamic stability theory, and a considerable number of works have addressed certain idealized configurations, e.g. [103, 43, 67, 107]. Common assumptions in these works include

- time-independent basic flow with parallel streamlines,
- axisymmetric or two-dimensional perturbations,
- inviscid flow and

- temporal stability analysis.

The simplest formulations are achieved by by incorporating most or all of these assumptions. In particular, the first assumption reduces the stability problem to one inhomogeneous direction in space, and is therefore almost universally adopted. The relaxation of these modeling assumptions has progressed incrementally but is far from complete. The contributions of the author on the instability of two-phase shear layers are part of these ongoing efforts. Linear stability results for this problem also furnish a valuable test case for computational methods for multiphase flow. The next sections give an overview of the linear stability calculations by the author and their use in the verification of an improved viscosity approximation in the Volume-of-Fluid code SURFER [62].

4.2 Linear stability results

4.2.1 Basic assumptions

Linear stability results for two-phase shear layers were obtained by the author in close collaboration with S. Zaleski. They are described in two publications [7, 8]. The focus is on the effects of viscosity and of approximate basic velocity distributions in two-dimensional, temporal stability analysis. The use of temporal stability analysis can be justified when the instability grows slowly in comparison with the time scale of advection [51, 33].

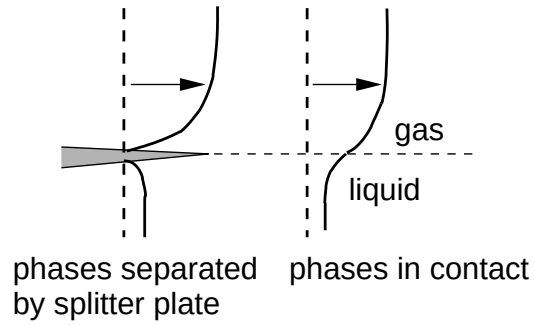

Figure 15: *Compensation of the velocity defect with increasing downstream distance from the splitter plate. Only the velocity distribution close to the interface is considered in the formulation of the stability problem.*

The flow geometry under consideration is sketched in Fig. 15. It retains only the essential features of the problem, namely two parallel streams of gas and liquid coming into contact at the tip of a splitter plate. The two fluids have constant velocities at large distance from the interface, i.e. the effect of outer boundaries is neglected. At the tip of the splitter plate the velocity distribution is characterized

by boundary layers and a velocity defect, which are caused by the no-slip boundary condition. The velocity defect will be compensated at some distance from the plate because the liquid is accelerated through shear exerted by the fast gas stream. The velocity distribution should then approach the defect-free shape illustrated in Fig. 15 on the right. Only such "relaxed" profiles are fully compatible with the assumption of essentially time-independent basic flow in linear stability theory, and they have therefore been considered exclusively. This point is also further discussed in the publications [7, 8].

4.2.2 Viscous effects [7]

In the publication [7], the influence of viscosity on the linear instability is examined systematically by comparing viscous and inviscid calculations. The basic velocity profiles for this study are shown schematically in Fig. 16. In the viscous case, the basic velocity distribution is composed of an error function in each phase, which are centered on the interface, i.e.

$$U_{\text{liquid}} = U^{(0)} + U_l \,\mathrm{erf}(y/\delta_l), \quad (y < 0), \tag{20}$$

$$U_{\text{gas}} = U^{(0)} + U_g \,\mathrm{erf}(y/\delta_g), \quad (y > 0). \tag{21}$$

This choice of velocity profile is made because of the distant resemblance of the configuration with the first Stokes problem, i.e. parallel flow with cross-stream momentum diffusion caused by an impulsively started, flat boundary. The velocity profile in the Stokes problem is given by an error function.

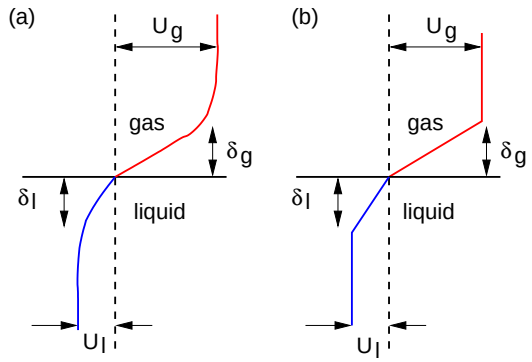

Figure 16: *Basic velocity profiles with boundary layers on the interface. The viscous stability problem requires a smooth profile (a). A piecewise linear profile (b) is used for the inviscid case. Boundary layer thicknesses and asymptotic velocities are the characteristic features.*

For the inviscid calculations, this error function profile has been simplified to a broken-line profile with identical main features, i.e. boundary layer sizes and asymptotic velocities. The simplification allows one to find an analytic dispersion relation

because the Rayleigh equation can be solved by exponentials when the velocity profile is linear. Single-phase calculations have shown that temporal stability results are fairly insensitive to such modifications.

Non-dimensional parameters of the viscous problem are the ratios

$$r = \rho_g/\rho_l, \quad m = \mu_g/\mu_l, \quad n = \delta_g/\delta_l \tag{22}$$

of densities, viscosities and boundary layer thicknesses as well as the Reynolds and Weber numbers based on the gas layer, i.e.

$$We = \frac{\rho_g U_g^2 \delta_g}{S}, \quad Re = \frac{\rho_g U_g \delta_g}{\mu_g}, \tag{23}$$

where S denotes the surface tension. The velocity ratio U_g/U_l is determined by the shear balance

$$\frac{\mu_l U_l}{\delta_l} = \frac{\mu_g U_g}{\delta_g}. \tag{24}$$

on the interface, which implies

$$\frac{U_g}{U_l} = \frac{n}{m} \tag{25}$$

This relation is also imposed for the broken-line profile although there is no shear on the interface in the inviscid case.

The formulation of the Orr-Sommerfeld and Rayleigh equations as complex linear eigenvalue problems for the streamfunction perturbations

$$\psi_{\text{liquid}}(x,y,t) = \exp(i\alpha(x-ct))\phi_l(y) \quad (y<0), \tag{26}$$

$$\psi_{\text{gas}}(x,y,t) = \exp(i\alpha(x-ct))\phi_g(y) \quad (y>0). \tag{27}$$

with given wavenumber α is described in [7]. In the inviscid case, the complex eigenvalues $c(\alpha)$ are obtained by solving the polynomial dispersion relation with the Maple computer algebra package. In the viscous case, the Orr-Sommerfeld equations are discretized by a Chebyshev collocation method, and the resulting general algebraic eigenvalue problem is solved with a NAG library function. Of interest are mostly the unstable modes, i.e. eigenvalue branches $c(\alpha)$ with positive imaginary part.

Surface tension opposes the deformation of the interface and thereby provides a damping influence. In [7] it is therefore mostly neglected in order to observe all possible inviscid and viscous instability mechanisms. Different physical mechanisms lead to multiple unstable branches, but these modes are usually "mixed", i.e. affected by more than one of the instability mechanisms. Systematic changes in the parameters such as r and Re can therefore be useful to clarify the nature of these unstable modes. This approach is followed in [7]. The nondimensional results discussed below are based on the lengthscale δ_g and velocity scale U_g.

Major differences between viscous and inviscid cases can be identified from the growth rates αc_i in Fig. 17 for parameters r and m close to the pairing air/water. The

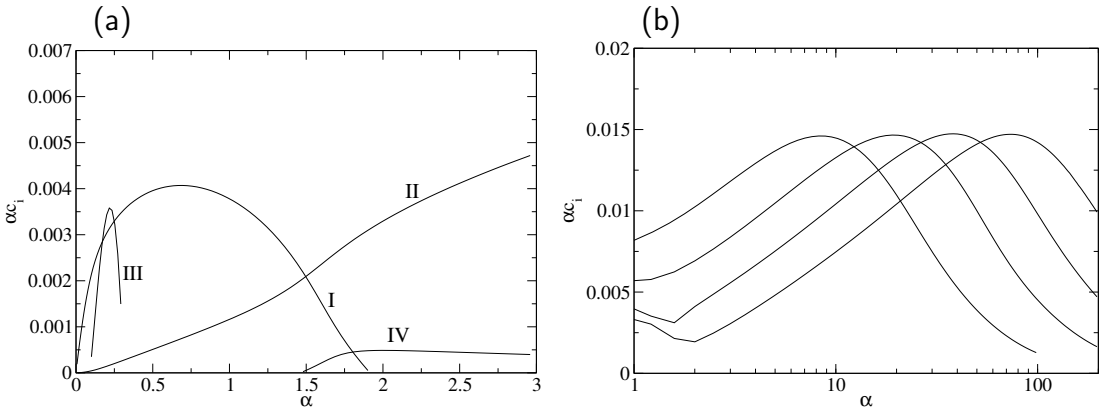

Figure 17: *Viscous stability results for* $n = 1$, $r = 0.0012$, $m = 0.012$*: (a) unstable modes for* $Re = 6\times10^4$*; (b) for* $Re = 2000$, $Re = 10^4$, $Re = 4\times10^4$, $Re = 1.6\times10^5$ *in the high-wavenumber range. Surface tension is neglected.*

multiple unstable branches in Fig. 17(a) are not found in inviscid calculations, where only an unstable branch in the vicinity of mode I appears. The other branches II, III, IV are therefore caused by viscosity, and are sensitive to changes in Re. By variation of Re it turns out that mode IV is not the result of a distinct viscous instability mechanism but rather of "mode mixing" between the inviscid mode and damped viscous modes. However, branch III appears to be caused by the Tollmien-Schlichting mechanism, i.e. the destabilization of a neutral mode by viscous diffusion, because it becomes weaker and its peak shifts to smaller α with increasing Re [38].

The most significant result is the appearance of mode II. Its peak retains its amplitude but shifts to larger values of α (Fig. 17(b)). The wavenumber of the peak grows in proportion with $\sqrt{Re}$. This scaling is caused by a purely viscous instability identified by Hooper and Boyd [50] for plane and unbounded two-fluid Couette flow. Its physical mechanism was later explained by Hinch [48]. The velocity profile in the present configuration is equivalent to such a Couette flow near the interface provided that the instability lengthscale is small compared with the boundary layer. The mode II associated with this instability is called the H mode in [7] to acknowledge the authors Hooper and Hinch.

The time scale of the H mode is set by the inverse shear rate $\mathcal{S}^{-1} = \delta_g/U_g$ at the interface. Since the unbounded Couette flow lacks an intrinsic length scale, the lengthscale of the H mode is then set by viscous diffusion during the characteristic instability time $\mathcal{S}^{-1}$, i.e. $\sqrt{\nu_g\mathcal{S}^{-1}} = \delta_g/\sqrt{Re}$. This lengthscale differs by the factor $1/\sqrt{Re}$ from the chosen unit length δ_g used above, and thereby accounts for the scaling of the most unstable wavenumber of the H mode with $\sqrt{Re}$.

The physics of the H mode is not obvious. The starting point is a weak sinusoidal interface deformation, which gives rise to vorticity perturbations because of the continuity of tangential velocity and shear stress on the interface. The perturbation

vorticity is advected differentially by the mean shear, and can thereby sustain and amplify the interface deformation. This process does not require fluid inertia. The finer points of this instability mechanism are analyzed and explained by Hinch [48].

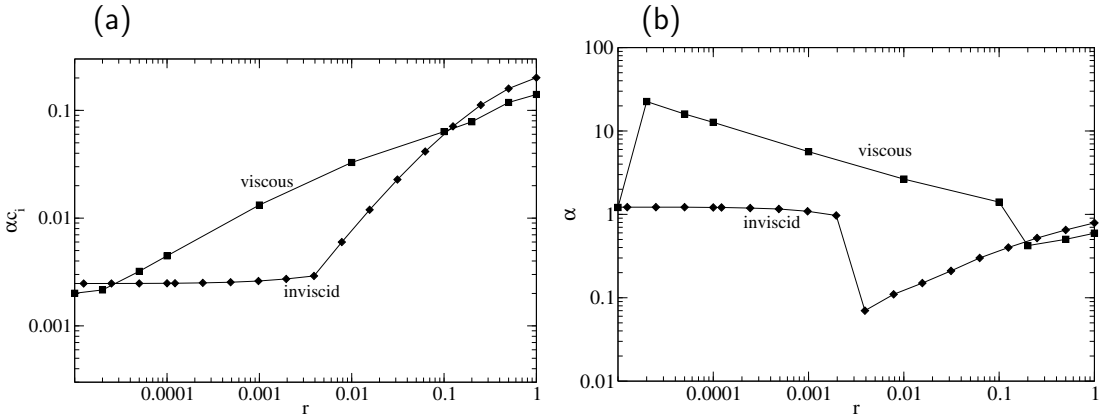

Figure 18: *Maximum growth rate and corresponding wavenumber as function of the density ratio r for $m = 0.01$, $n = 1$. Surface tension is neglected.*

For a given viscosity ratio, the H mode can provide higher maximum growth rates than the inviscid Kelvin-Helmholtz mechanism over a fairly large range of density ratios. This is illustrated by Fig. 18, which shows the maximum growth rate αc_i and the corresponding wavenumber α from viscous and inviscid calculations for $m = 0.01$ and $n = 1$. The velocity profile is not affected by the density ratio r. For r close to unity and very small values below 10^{-4} the inviscid mechanism dominates because the growth rates from the inviscid case are slightly larger than those of the viscous case, and the wavenumbers with maximum growth rate are close between the two cases. For moderate r the H mode dominates. It provides larger growth rates at smaller wavenumbers. The inviscid growth rate is reduced with decreasing r because the inviscid instability is driven by the dynamic pressure in the gas phase. It finally reaches a plateau below $r \approx 0.005$ because at such low r the effect of the gas phase is no longer felt in the liquid. The instability is then merely that of the liquid boundary layer with a free surface.

The damping influence of surface tension affects the H mode preferentially because it typically acts at smaller lengthscales than the other instabilities. Even at fairly large We it is therefore already partly suppressed, but it can nonetheless cause noticeable differences between viscous and inviscid growth rates. This is demonstrated in [7] for parameters corresponding to air/water atomization experiments [73]. The need for viscous stability analysis in such problems on account of the H mode is the main conclusion of [7].

4.2.3 Basic flow profiles from boundary layer theory [8]

The basic velocity profiles for the stability calculations in [7] are physically plausible but they are not justified by a self-contained mathematical model. This lack of a mathematical foundation is perhaps not too severe in view of the numerous additional assumptions that have to be made in the analysis, but it is nonetheless a weak point that should be addressed. The publication [8] is concerned with this issue. It replaces the error function profiles by solutions of the two-fluid boundary layer model proposed by Lock [71], and compares the stability results when error function profiles are appropriately matched to the profiles from boundary layer theory. The deficiencies of this approach are that the flow in the nozzle or along the splitter plate is replaced by uniform streams, and that the absolute boundary layer thickness remains indeterminate. As in other boundary layer problems, it grows as $\sqrt{x}$ with the streamwise coordinate x.

The non-dimensional parameters in the two-fluid boundary layer model are the density- and viscosity ratios r and m and the asymptotic velocity ratio

$$\lambda = \frac{U_{\text{liquid}}(y \to -\infty)}{U_{\text{gas}}(y \to +\infty)}. \tag{28}$$

The boundary layer equations for this problem have been formulated by Lock [71], but they were only solved semi-analytically in the special case of a liquid layer at rest. In Ref. [8] they are solved numerically in each fluid, and the matching conditions for velocity and shear stress are satisfied by an iterative procedure. With the converged solution for the velocity profile one can then calculate the displacement thicknesses d_{liquid} and d_{gas} of the boundary layers in each phase. With the interface located at $y = 0$, these thicknesses are

$$d_{\text{gas}} = \frac{1}{U_{\text{gas}}(\infty) - U_{\text{gas}}(0)} \int_0^\infty (U_{\text{gas}}(\infty) - U_{\text{gas}}(y))\,\mathrm{d}y, \tag{29}$$

$$d_{\text{liquid}} = \frac{1}{U_{\text{liquid}}(0) - U_{\text{liquid}}(-\infty)} \int_{-\infty}^0 (U_{\text{liquid}}(y) - U_{\text{liquid}}(-\infty))\,\mathrm{d}y. \tag{30}$$

Fig. 19 shows the dependence of the ratio $n = d_{\text{gas}}/d_{\text{liquid}}$ for two parameter combinations corresponding roughly to air/water ($r = 0.001$, $m = 0.01$) and hydrogen/liquid oxygen ($r = 0.02$, $m = 0.025$). In both cases, the thickness ratio n changes noticeably for small λ, but it remains of the same order of magnitude.

The influence of the velocity profile on the stability results is examined in Ref. [8] by comparison with error function profiles (20,21) with the same displacement thicknesses and matching velocities $U^{(0)} = U_{\text{gas}}(0) = U_{\text{liquid}}(0)$ on the interface. Fig. 19(b) shows a satisfactory agreement of growth rates based on the velocity profile from two-fluid boundary layer theory (called *exact* in the legend) and on the matching composite error function profile (called *approximate* in the legend). The velocity ratio in Fig. 19(b) is $\lambda = 0$, i.e. the liquid is at rest. For larger values of λ the agreement

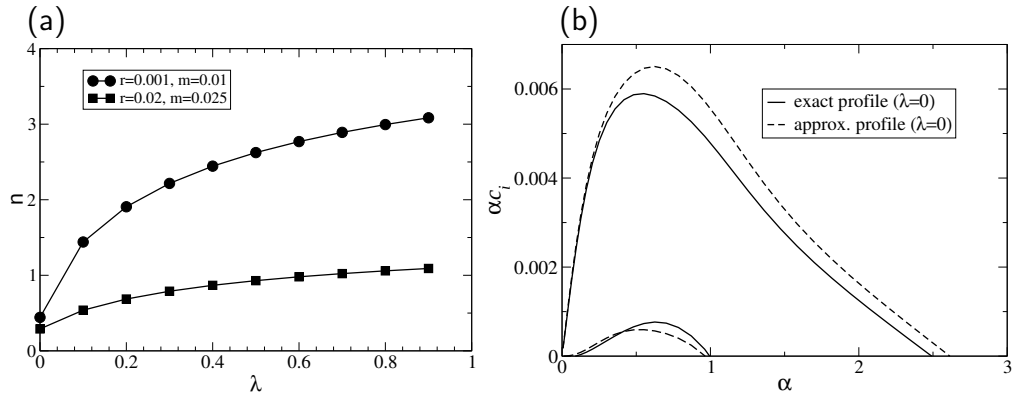

Figure 19: *(a) Ratio n of displacement thicknesses from the two-fluid boundary layer model as function of the asymptotic velocity ratio; (b) temporal stability results for exact and approximate velocity profiles (20,21) for $r = 0.001$, $m = 0.01$, $Re = 500$, $We = 10$. Re and We are based on the gas properties and U_g, δ_g.*

becomes closer. At $\lambda = 0.9$ the differences are no longer visible when the results are plotted as in Fig. 19(b). The results for $r = 0.02$, $m = 0.025$ display identical trends. In conclusion, the use of boundary layer theory does not lead to qualitative differences in the temporal stability results obtained in [7].

4.3 Direct numerical simulations [9]

Two-phase flows with large density and viscosity ratios r and m still represent a challenge for direct numerical simulations (DNS). The linear instability of a two-phase shear layer is therefore an important test case for such codes. It can be studied in two-dimensional simulations. The author has implemented this test case in the DNS code SURFER, which has been developed by S. Zaleski and his co-workers [62, 44].

SURFER is based on the Volume-of-Fluid (VOF) approach. The two phases are represented as one fluid with variable properties on a fixed grid. The two fluids are distinguished by a characteristic function. It takes the values 0 or 1 depending on the presence of one or the other phase at the given location in space. The discrete analog of this function is the volume fraction or color function C, which represents the fraction of the grid cell occupied by one of the phases. The VOF method tracks the interface implicitly through the color function, which is advected with the flow. The advantage of this approach is that it captures topology changes automatically. This is a major difficulty in explicit interface tracking by connected markers, where the geometry of the interface has to be monitored and the topology is changed by breaking and/or reconnecting different parts of the interface mesh [101, p. 56].

However, this advantage of VOF methods in the handling of topology change does not come for free. In contrast to markers, the VOF methods require considerable effort for proper interface advection. It particular, the interface must be reconstructed in

each time step, i.e. the interface position must be calculated in "cut" grid cells partly occupied by both phases. Apart from this kinematic problem, the cut cells also require effective values for the material properties density and viscosity for time advancement of the discretized Navier-Stokes equations, which are treated with finite differences and a projection algorithm in SURFER [62].

For the interpolation of the density in cut cells the arithmetic mean

$$\rho = C\rho_{\text{liquid}} + (1 - C)\rho_{\text{gas}} \tag{31}$$

is clearly appropriate (additivity of mass). For the interpolation of viscosity there is no such obvious answer. The arithmetic mean is frequently chosen for simplicity, but it can be advantageous to use the harmonic mean

$$\frac{1}{\mu} = \frac{C}{\mu_{\text{liquid}}} + \frac{1 - C}{\mu_{\text{gas}}}. \tag{32}$$

The effect of these different viscosity interpolations in SURFER on the linear evolution of the two-phase shear layer instability has been studied by the author in collaboration with S. Zaleski, P. Yecko and A. Bagué in [9]. This parametric study shows that the harmonic mean is superior to the arithmetic mean, and that SURFER can reproduce the linear growth rates from the stability calculations over a wide range of density and viscosity ratios.

The harmonic mean of the viscosity has been used in earlier work by Coward et al. [32] on two-layer Taylor-Couette flow. The argument leading to the harmonic mean for viscosity is similar to that for the effective thermal conductivity in one-dimensional heat conduction when the conductivity is discontinuous across an interface [82, sec 4.2-3]. In this case, the heat flux across the interface is continuous, but the temperature gradient is not. The effective heat conductivity λ_{eff} is then given by

$$\frac{d_1 + d_2}{\lambda_{\text{eff}}} = \frac{d_1}{\lambda_1} + \frac{d_2}{\lambda_2}, \tag{33}$$

where d_1 and d_2 are the thicknesses of the layers 1 and 2 with thicknesses d_1 and d_2. In two-phase flow, the analog of the heat flux and temperature gradient are the shear stress and the shear rate, respectively. The harmonic mean (32) is then a direct consequence of eq. (33). It should be noted that the harmonic mean is based on an essentially one-dimensional configuration and does not account for the full set of balance conditions for velocity and stress at the interface.

The effect of the viscosity interpolation in SURFER is explored in two-dimensional simulations with periodic boundary conditions in x. The simulations are initialized with the basic velocity profile given by (20,21) and an added unstable eigenmode (26,27) from linear stability calculations. According to linear theory, the position $y = H(x, t)$ of the interface evolves as

$$H(x, t) = A(t) \cos(\alpha x - \beta), \tag{34}$$

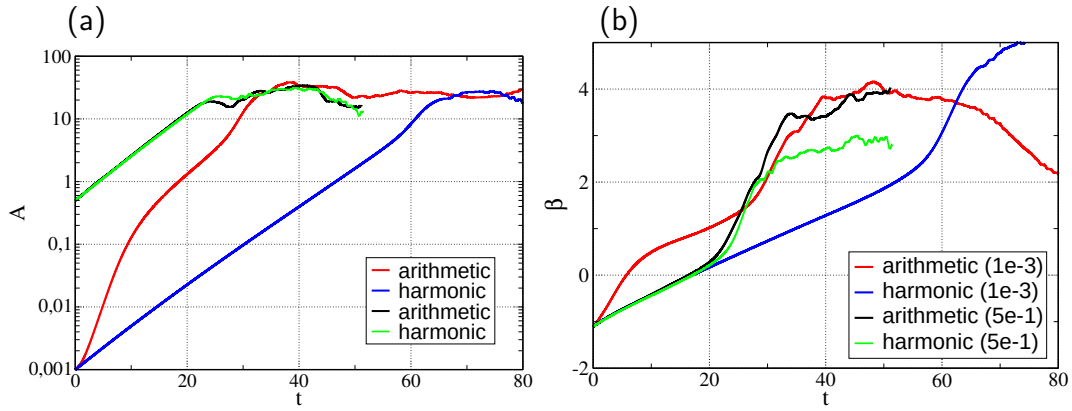

Figure 20: *SURFER results for $r = 0.02$, $m = 0.02$, $n = 1$: amplitude A (a) and phase β (b) for arithmetic and harmonic mean and different initial amplitudes. A is normalized to the mesh size. The Reynolds number based on gas velocity and boundary layer thickness is $Re = 2000$. Surface tension is neglected.*

where the amplitude A and phase angle β satisfy the relations

$$A(t) = A_0 \exp(\alpha c_i t), \quad \beta = \alpha c_r t + \beta_0 \tag{35}$$

The interface position in the simulation is reconstructed by adding the color function over vertical grid columns, and the amplitude and phase angle are obtained by Fourier transform of the function $H(x,t)$. Boundary layers of the basic velocity profile are well resolved by the numerical grid.

Fig. 20 shows that linear stability results and simulation results differ for the arithmetic mean if the initial amplitude of the interface modulation is significantly smaller than one grid cell (red lines: arithmetic ($A = 10^{-3}$)). Possible modifications of nonlinear results by the arithmetic mean are also apparent in this case. However, the effect of the overpredicted viscosity in the cut cells ceases to be important as soon as the amplitude reaches the dimensions of a grid cell. The correct growth rate and phase velocity are then almost recovered. With large initial amplitudes ($A = 0.5$ in Fig. 20), the different viscosity interpolations provide essentially identical exponential growth in good agreement with linear stability theory. In further simulations with the harmonic mean, good agreement for growth rates and phase velocities with linear stability theory was obtained for the two viscosity ratios $m = 0.1$, $m = 0.02$ and density ratios in the range $0.005 \leq r \leq 1$.

The effect of surface tension and Reynolds number on the formation of ligaments and droplets in the nonlinear stage is the focus of the publication [20]. The contribution of the author to this work is mainly the code validation with the unstable modes as explained above. In [20] it is demonstrated that the formation of ligaments and droplets requires fairly large Reynolds and Weber numbers. However, the ligaments stretch to unrealistic lengths because of the absence of transverse instabilities in the two-dimensional simulations.

4.4 Summary

The accurate modeling and simulation of the complex phenomena in two-phase shear layers remains a challenge for theory and computation. The publications [7, 8] have drawn attention to the potential role of the viscous H mode in the linear stage of the destabilization of the liquid-gas interface. Viscosity has been frequently neglected in this context because of the high Reynolds numbers and because the flow is inviscidly unstable. The H mode had been previously considered mainly in the context of two-layer channel flow at small Reynolds numbers. In [7] the H mode is clearly identified on the basis of its dependence on the Reynolds number. This aspect is missing in [107].

Viscous stability results are also required for the validation of DNS codes for two-phase flows. The original motivation for the stability studies [7, 107] came from tests with the SURFER code, which failed to provide satisfactory results because of the use of inviscid stability theory with a discontinuous velocity profile and the arithmetic mean for the viscosity approximation. The proper representation of the shear balance on the interface has not only been an issue with SURFER [9, 20]. Other authors have recently considered this aspect for another class of numerical methods for two-phase flows [94, 79].

5 Magnetohydrodynamic channel flows

5.1 Introduction

The interaction of magnetic fields with conducting fluids is of considerable interest in geo- and astrophysics, but also for industrial and laboratory applications. Among the latter are the pumping and stirring of liquid metals by magnetic fields in metallurgical plants [34], magnetic brakes in continuous casting of steel [100] and magnetic damping of melt flow in crystal growth [104]. In addition to these desired interactions, ambient magnetic fields can lead to an undesirable magnetohydrodynamic instability in the Hall-Héroult electrolysis cells for primary aluminum production [35, ch. 11]. A minimum layer thickness of the highly resistive electrolyte layer is required to aviod this instability, which limits the energetic efficiency of this process. The suppression of turbulence by strong magnetic fields also hinders efficient turbulent heat transport in liquid metal blankets for the toroidal plasma chamber of future fusion reactor designs [27]. The study of turbulent magnetohydrodynamic flows of liquid metals is therefore not only of fundamental interest but also important from an application perspective.

The theoretical and experimental investigation of liquid metal flows under the influence of an imposed magnetic field began with the pioneering work by Hartmann around 1937. On the theoretical side, he obtained the laminar solution for channel flow with transversal magnetic field [46]. Together with Lazarus he also took measurements of the pressure loss in pipe and duct flow with a transversal magnetic field [47]. Using mercury as working fluid, they verified the laminar friction law predicted by Hartmann's theoretical work. They also detected transition to turbulence through departures from the laminar friction law, and studied a variety of geometrical shapes of the cross-section of the pipes. Later work by Murgatroyd [77] improved the experimental accuracy of the pressure loss measurements, and provided critical parameters for the transition to turbulence in magnetohydrodynamic duct flow. Similar experiments with increasing complexity were performed subsequently by numerous groups in the Soviet Union, Western Europe and the US in the 1960s and 1970s. These developments were accompanied by efforts on the theoretical side to understand the influence of magnetic fields on instability and turbulence. The theoretical studies focused on geometrically simple flows such as homogeneous turbulence and simple wall-bounded geometries. In particular, the linear stability problem for the laminar Hartmann flow (channel flow with transversal magnetic field) was studied by several authors, and simple closure models for the turbulent Hartmann flow were developed [25].

In recent years, numerical simulations have played an increasingly important role in the study of magnetohydrodynamic flows [58]. Direct numerical simulations have explored the anisotropic features of homogeneous turbulence in periodic computational domains, and in simple wall-bounded flows [108, 56, 89]. In addition, turbulence models on the basis of the Reynolds-averaged Navier-Stokes equations and subgrid-scale models for large-eddy simulation have been adapted and tested for such flows

[57, 59, 55]. The work presented here is a part of these broader efforts in the numerical study of magnetohydrodynamic turbulence. In particular, the author has contributed to a numerical study of turbulent Hartmann flow and to a study of transition to turbulence in magnetohydrodynamic channel flow with spanwise magnetic field. The following sections give an overview of this work.

5.2 Basic equations and numerical method

Conducting flows in a time-independent magnetic field $\boldsymbol{B}$ are affected by the Lorentz force $\boldsymbol{j} \times \boldsymbol{B}$ caused by the induced current density $\boldsymbol{j}$ in the fluid. The body force term $\boldsymbol{j} \times \boldsymbol{B}$ has to be added to the Navier-Stokes equations (1). In comparison with the applied field $\boldsymbol{B}$, the induced magnetic field $\boldsymbol{b}$ associated with $\boldsymbol{j}$ is usually fairly small for the typical dimensions and velocities of conducting flows in the laboratory and in technological applications. It can therefore be neglected in the Lorentz force term. To the same order of approximation, the electric field in the conducting fluid can be expressed by a potential gradient $-\nabla\Phi$. Ohm's law for a moving conductor is then given by

$$\boldsymbol{j} = \sigma \left(-\nabla\Phi + \boldsymbol{v} \times \boldsymbol{B}\right), \tag{36}$$

where σ denotes the electric conductivity. The high conductivity of liquid metals ensures that the fluid remains electrically neutral, i.e. the charge density is zero on macroscopic time scales. For this reason, the current density is solenoidal, and one can find the electric potential from the condition

$$0 = \frac{\nabla \cdot \boldsymbol{j}}{\sigma} = -\nabla^2\Phi + \nabla \cdot (\boldsymbol{v} \times \boldsymbol{B}). \tag{37}$$

Eq. (36,37) represent the so-called quasistatic approximation based on the electric potential [35]. The appendix contains a more systematic derivation from the full induction equation by an expansion in the magnetic Reynolds number.

In summary, the mathematical model for conducting flows is given by

$$\frac{\partial \boldsymbol{v}}{\partial t} + (\boldsymbol{v} \cdot \nabla)\boldsymbol{v} = -\frac{\nabla p}{\rho} + \nu\nabla^2\boldsymbol{v} + \frac{\sigma}{\rho}\left(-\nabla\Phi + \boldsymbol{v} \times \boldsymbol{B}\right) \times \boldsymbol{B}, \tag{38}$$

$$\nabla \cdot \boldsymbol{v} = 0, \tag{39}$$

$$\nabla^2\Phi = \nabla \cdot (\boldsymbol{v} \times \boldsymbol{B}). \tag{40}$$

Boundary conditions for the channel geometry are zero velocity conditions on the walls located at $z = \pm L$. The channel walls are assumed to be insulating throughout this section, whereby the normal current density j_z vanishes for $z = \pm L$, and thereby the normal derivative of the electric potential.

As for Marangoni convection, the numerical studies have been performed with pseudo-spectral methods based on Fourier-Chebyshev modal expansions of the hydrodynamic fields. The extension of the corresponding parallel code from the doctoral thesis of the author [19] is described in the papers [60, 11]. The additional

computational effort for the Lorentz force is fairly small since the term requires no additional Fourier transforms. The Poisson equation for the electric potential causes negligible computational cost because it decouples for different wavevectors $\boldsymbol{k}$, and only one-dimensional Helmholtz equations have to be solved.

5.3 Turbulent Hartmann flow [10]

5.3.1 Parameters and equations

For non-magnetic laminar channel flow the driving pressure gradient is exclusively compensated by viscous forces. When a wall-normal magnetic field is applied, then electric currents are induced in the spanwise direction, and the associated Lorentz force opposes the flow. Provided the induced currents are sufficiently strong, the Lorentz forces dominate over the viscous forces, and the uniform driving pressure gradient is almost exclusively compensated by the Lorentz forces. In this situation a uniform (plug) velocity profile is established in place of the parabolic Poiseuille profile. The uniform velocity profile adjusts to the no-slip condition at the channel wall in a boundary layer characterized by a balance of viscous and Lorentz forces. This so-called Hartmann boundary layer has a thickness of order δ, which is determined by the balance of viscous and Lorentz forces. The viscous forces in the Hartmann layer are of order $\rho\nu U/\delta^2$, where U is the bulk velocity. The induced currents are estimated by σUB, and the Lorentz force estimate is therefore σUB^2. By equating these two forces one finds

$$\delta = \frac{1}{B}\sqrt{\frac{\rho\nu}{\sigma}}. \tag{41}$$

The corresponding dimensionless parameter is the Hartmann number

$$Ha = LB\sqrt{\frac{\sigma}{\rho\nu}} = \frac{L}{\delta}. \tag{42}$$

It also characterizes the ratio of Lorentz forces to viscous forces for a characteristic lenghtscale L of the flow, which is customarily chosen as the half-channel width in the case of channel flow.

The mean velocity distribution $u(z)$ satisfies the streamwise momentum equation

$$\rho\nu\frac{\partial^2 u}{\partial z^2} + \frac{\partial \tau_T}{\partial z} - \sigma B^2\left(u - U_{\mathrm{av}}\right) - \frac{\partial p}{\partial x} = 0. \tag{43}$$

This equation applies for turbulent flow as well as for laminar flow. In the latter case the fluctuating streamwise and wall-normal velocity components u' and w' are absent, and the turbulent stress $\tau_T(z) = -\rho\langle u'w'\rangle$ vanishes.

The Lorentz force term is $-\sigma B_0^2\left(u - U_{\mathrm{av}}\right)$, where U_{av} denotes the mean velocity in the channel. As a consequence, the total Lorentz force turns out to be zero. Eq. (43) can also be written as $\mathrm{d}\tau/\mathrm{d}z = \partial p/\partial x$, where τ is the sum of the viscous stress

$\tau_v = \rho\nu \mathrm{d}u/\mathrm{d}z$, the turbulent stress τ_T and the electromagnetic stress τ_m representing the integrated Lorentz force term in eq. (43). As in ordinary channel flow, the total stress τ is an antisymmetric linear function with respect to the middle of the channel.

The solution of eq. (43) in the laminar case is

$$u(z) = U_0 \frac{\cosh(Ha) - \cosh\left(Ha\, z/L\right)}{\cosh(Ha) - 1}, \tag{44}$$

where U_0 is the center-plane velocity and the channel walls are located at $z = \pm L$. For $Ha \gg 1$, the velocity profile approaches the asymptotic form

$$u(z) = U_0 \left(1 - \exp(-z'/\delta)\right), \tag{45}$$

where z' denotes the distance from the wall. Instabilities of this velocity distribution due to mean shear must therefore originate in the Hartmann layer, and the appropriate instability parameter is the Reynolds number

$$R = \frac{U_0 \delta}{\nu} = \frac{U_0 L/Ha}{\nu} = \frac{Re}{Ha} \tag{46}$$

based on δ and U_0.

The linear instability of the laminar Hartmann flow has been considered by several authors [95, 70]. The critical value for exponentially growing perturbations is $R_c \approx 48000$. This value is far larger than the values $R \approx 200 \ldots 400$, at which transition to turbulence is found in experiments. Significant gaps between theoretical and experimental instability thresholds are also found in other, non-magnetic shear flows. These apparent contradictions have been partly resolved in recent years by the development of new concepts in stability theory [91]. For Hartmann flow, a two-step transition mechanism was considered by Krasnov et al. [60]. It is based on transient linear growth of non-modal perturbations, which are then destabilized by random noise. This numerical study provides a critical value $R_c \approx 400$, which is in good agreement with $R_c \approx 380$ found in the recent experiment by Moresco and Alboussière [76].

Based on these results, a systematic study of the effects of R and Ha on turbulent mean flow properties was undertaken by the present author in collaboration with D. Krasnov and E. Zienicke. The main results have been reported in the publication [10]. The following discussion summarizes the main points.

5.3.2 Mean flow properties

The direct numerical simulations were performed for $R = 450$, $R = 500$, $R = 700$ and $R = 900$ with four different values of Ha for each of these R. These extensive parallel computations required several 10000 hours of mono-processor time to obtain sufficiently converged statistics. The computational rescources were provided mainly

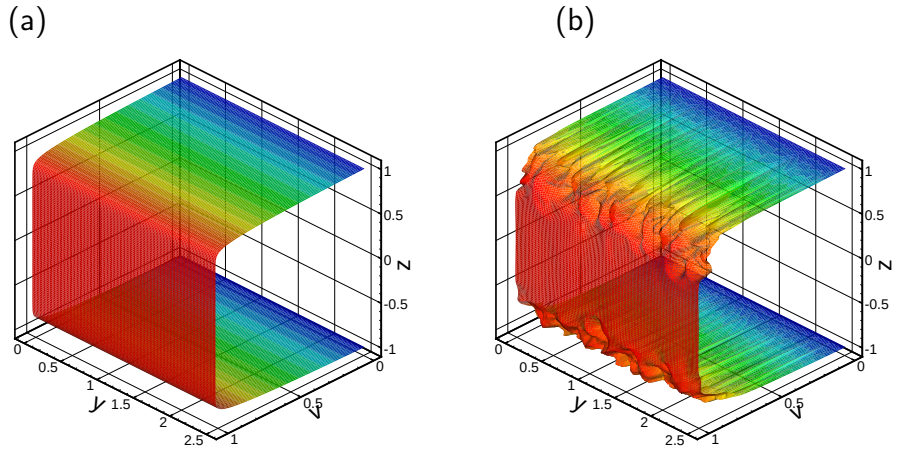

Figure 21: *Velocity distribution $v_x(y,z)$ in a vertical plane for Hartmann flow at $Ha = 30$: (a) laminar flow, (b) snapshot of turbulent flow at $R = 500$.*

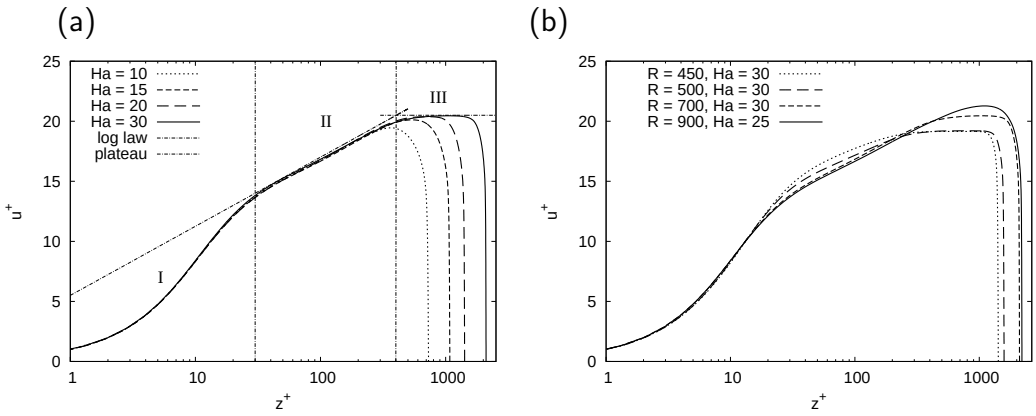

Figure 22: *Mean velocity profiles normalized with u_τ and ν/u_τ. For fixed R the plateau grows with increasing Ha, while increasing R leads to a wider logarithmic interval. The profiles are drawn across the entire channel in order to highlight the plateau.*

by the von Neumann Institute for Computing at the research center Jülich through a grant application.

In the simulations the mean velocity $U_{\rm av}$ is prescribed, i.e. the simulations run with constant volume flux in the channel. The two velocities $U_{\rm av}$ and U_0 are related by the equation

$$U_{\rm av} = U_0 \frac{\cosh(Ha) - \sinh(Ha)/Ha}{\cosh(Ha) - 1} \sim U_0 - \frac{U_0}{Ha}, \tag{47}$$

which is obtained from integration of the laminar velocity profile (44). One can also define a Reynolds number $R_{\rm av}$ based on $U_{\rm av}$ instead of R based on U_0.

Fig. 21 shows that the turbulence does not spread to the bulk provided that Ha is large enough. However, the turbulent Hartmann layers become broader by comparison with their laminar counterparts. As a consequence, the average turbulent velocity profile appears more rounded than the laminar one. This is in contrast with ordinary channel turbulence, where the turbulent mean profile is considerably steeper near the walls than the parabolic laminar profile. Animations of fluctuating velocity distributions as shown in Fig. 21(b) have been prepared by D. Krasnov in the course of our joint work on this problem. The author submitted them to Prof. G. Homsy, who is the editor of the educational DVD "Multimedia Fluid Mechanics". They are included in the second edition of this DVD, which was published in 2008 [49].

In hydrodynamic channel turbulence it is customary to work with friction units. They are based on the wall shear stress $\tau_w = L\partial p/\partial x$, which is used to define the friction velocity u_τ by

$$\rho u_\tau^2 = \tau_w = L\partial p/\partial x. \tag{48}$$

The friction length is therefore ν/u_τ, and the friction Reynolds number is $Re_\tau = u_\tau L/\nu$. These units will be used in what follows. Dimensionless quantities in friction units are indicated by the superscript $+$.

The influence of the parameters R and Ha is illustrated in Fig. 22, where semi-logarithmic plots of the mean velocity are presented. In Fig.22(a) one can identify three different regions in the profiles. A viscous sublayer (with $u^+ \sim z^+$) marked as region I is followed by a logarithmic layer (with $u^+ \sim A\log(z^+) + B$) marked as region II, which starts around $z^+ \sim 30 \ldots 40$. The plateau region marked III is formed at sufficiently large Ha. The profiles for different Ha then essentially coincide except for the width of the plateau.

Fig. 22(b) compares the profiles at the highest Ha for each R. One sees clearly that that the logarithmic range becomes wider as R increases, and that the plateau shrinks upon increasing R for $Ha = 30$. For $R = 900$ and $Ha = 25$ a plateau is barely present. From $R = 450$ to $R = 700$ the slope A increases whereas the offset B decreases. The differences between $R = 700$ and $R = 900$ in the logarithmic range are only slight. At $R = 900$ and $Ha = 25$ the values $A = 2.4$ and $B = 5.65$ provide a good fit.

The persistence of the logarithmic layer with a slope and offset in fair agreement with the hydrodynamic case suggests that the influence of the Lorentz forces on the turbulent fluctuations is rather weak in the turbulent Hartmann layers. This argument was already made by Alboussière and Lingwood, and they consequently proposed the use of the classical mixing length model for the turbulent stress [15]. As detailed in the publication [10], the turbulent stresses are better matched by the older model by Lykoudis and Brouillette [72], which introduces some additional correction terms in the mixing length ansatz. However, both models fail to represent the relatively rapid transition from the logarithmic layer to the the plateau region, and they overpredict the turbulent stress considerably. These deficiencies appear to be inherent in the mixing-layer approach and demonstrate the need for more sophisticated turbulence

models even in this simplest wall-bounded flow.

5.3.3 Friction coefficient

From a purely engineering viewpoint, the closure of the mean momentum equation (43) by a model term for the turbulent stress τ_T serves a single purpose, which is to predict the pressure loss or wall stress for given Re and Ha. In principle, this can also be accomplished if the velocity profile is known for given Re and Ha. This approach is tempting for the turbulent Hartmann flow in view of the pronounced three-layer structure of the mean velocity. It will therefore be briefly presented at this point.

From the previous results it is apparent that the parameter $R = Re/Ha$ determines the extent of the logarithmic layer in friction units when the plateau is present. However, the plateau may be absent if Ha is too low. In contrast to the laminar case the width of the turbulent Hartmann layer is also not simply determined by Ha. A separation of the turbulent Hartmann layers should appear when the ratio of electromagnetic and inertial forces exceeds a threshold value. The velocity scale in this case should be that of the fluctuations rather than the mean flow, i.e., it should be u_τ. The inertial forces can then be estimated as $\rho u_\tau^2 L$ and the Lorentz forces as $\sigma B^2 u_\tau$. The ratio is the interaction parameter

$$N_\tau = \frac{\sigma B^2 u_\tau}{\rho u_\tau^2 L} = \frac{Ha^2}{Re_\tau} \tag{49}$$

based on Re_τ. In summary, a plateau should be present if

$$N_\tau > N_c, \tag{50}$$

where the critical value N_c should be of order unity. This argument is not new, it can already be found in a less straightforward form in the book of Harris dated from 1960 [45]. It is also mentioned by Alboussière and Lingwood [15].

To predict the plateau velocity u_p for given R from this criterion one has to combine it with the logarithmic velocity profile

$$\frac{u_p}{u_\tau} = \frac{1}{\kappa} \ln\left(z_p' u_\tau/\nu\right) + B, \tag{51}$$

where z_p corresponds to the edge of the plateau. For critical conditions, i.e., $N_\tau = N_c$, the edge of the plateau is located in the middle of the channel at a wall distance $z_p' = L$. One can now make use of the definitions

$$N_c = \frac{Ha^2 \nu}{u_\tau L}, \qquad Ha = \frac{L}{\delta} \tag{52}$$

and the estimate $R = u_p \delta/\nu$ to express the argument of the logarithm in eq. (51) using R and u_p/u_τ only:

$$N_c = \frac{L\nu}{\delta^2 u_\tau} = \frac{L\nu u_p^2}{u_\tau R^2 \nu^2} = \frac{L u_\tau}{\nu} \frac{u_p^2}{R^2 u_\tau^2}. \tag{53}$$

If one replaces Lu_τ/ν in eq. (51) using the previous relation, one finds

$$\frac{u_p}{u_\tau} = \frac{1}{\kappa}\ln\left(N_c R^2 \frac{u_\tau^2}{u_p^2}\right) + B, \tag{54}$$

i.e. a relation for the velocity ratio u_τ/u_p, which contains the single parameter R. This relation can be rewritten in terms of the friction coefficient

$$c_f = 2\tau_w/\rho U_{\rm av}^2, \tag{55}$$

provided one makes the assumption that $U_{\rm av} \approx u_p$, i.e.,

$$u_p/u_\tau \approx U_{\rm av}/u_\tau = \sqrt{2/c_f}, \tag{56}$$

which is clearly justified for large Ha. The result is

$$\sqrt{2/c_f} = \frac{1}{\kappa}\ln\left(N_c R^2 c_f/2\right) + B, \tag{57}$$

i.e. a closed expression for the friction coefficient for given R in the limit $Ha \to \infty$.

The numerical results were obtained for relatively moderate Hartmann numbers. However, a direct comparison with the friction law (57) becomes possible by extrapolation of the friction coefficients from finite Ha to $Ha \to \infty$. The extrapolation can be justified by consideration of the streamwise momentum equation (43) in the following form

$$\frac{{\rm d}^2 u}{{\rm d}z^2} + \frac{{\rm d}\tau_{\rm T}}{{\rm d}z} - \frac{2}{R_{\rm av}^2 c_f}\left(u - \sqrt{2/c_f}\right) + \frac{1}{R_{\rm av} Ha}\sqrt{\frac{2}{c_f}} = 0 \tag{58}$$

based on friction units. This equation represents a nonlinear eigenvalue problem for c_f. The boundary conditions are $u = 0$ and ${\rm d}u/{\rm d}z = 1$ at $z = 0$ and ${\rm d}u/{\rm d}z = 0$ in the mid-plane of the channel at $z_m = R_{\rm av} Ha\sqrt{c_f/2}$. In this equation, Ha appears only in the nondimensional pressure term, and one can rewrite it as

$$R_{\rm av}\sqrt{c_f/2}\left(\frac{{\rm d}^2 u}{{\rm d}z^2} + \frac{{\rm d}\tau_{\rm T}}{{\rm d}z} - \frac{2}{R_{\rm av}^2 c_f}\left(u - \sqrt{2/c_f}\right)\right) = -\frac{1}{Ha} \tag{59}$$

If one assumes that the turbulent stress $\tau_{\rm T}$ does not depend on Ha, then the small parameter $1/Ha$ represents a linear perturbation term. Consequently, the leading terms in an asymptotic series for c_f would be

$$c_f \sim c_0(R_{\rm av}) + \frac{1}{Ha}c_1(R_{\rm av}), \tag{60}$$

i.e. linear in the small parameter. The problem with this argument is that the boundary condition ${\rm d}u/{\rm d}z = 0$ at $z_m = R_m Ha\sqrt{c_f/2}$ contains the parameter Ha

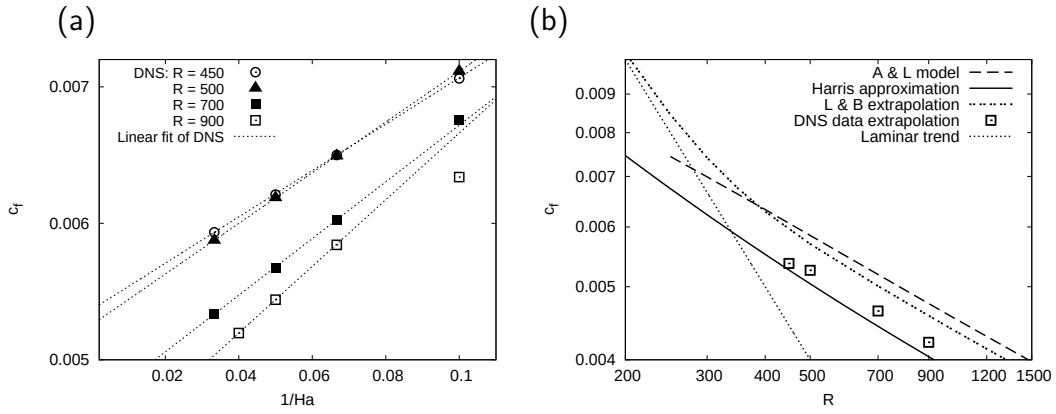

Figure 23: *Friction coefficients from direct simulations of turbulent Hartmann flow: (a) extrapolation to infinite Ha, (b) extrapolated values $c_f(R, Ha = \infty)$ in comparison with models and the laminar case.*

as well. On the other hand, the effect of z_m on c_f may become exponentially small when u itself decays exponentially for large z, in which case the expansion (60) might still work.

One can test the validity of the expansion (60) in the laminar case. The laminar friction coefficient can be calculated analytically from the definition of c_f together with eq. (44) and eq. (47). It is

$$c_f = \frac{2}{R_{\rm av}} \frac{\tanh(Ha)}{1 - \tanh(Ha)/Ha}, \tag{61}$$

which provides the limit $2/R_{\rm av}$ for infinite Ha. The first-order correction to this result is proportional to $1/Ha$ as one can see from an expansion of the right hand side. The hyperbolic tangent functions only provide exponentially small corrections.

The relation (60) does not apply directly to the simulation data, which have been obtained with the parameter $R = const$. The two parameters R and $R_{\rm av}$ are related by the formula

$$R_{\rm av} = R \frac{\cosh(Ha) - \sinh(Ha)/Ha}{\cosh(Ha) - 1} \sim R - \frac{R}{Ha} \tag{62}$$

when the Hartmann number is large. Assuming that the expansion coefficients of c_f in eq. (60) are continuously differentiable functions of $R_{\rm av}$, it is clear that dependence of c_f on $1/Ha$ for fixed R instead of fixed $R_{\rm av}$ is also linear for $Ha \to \infty$, i.e.

$$c_f \sim c_f^{(0)}(R) + \frac{1}{Ha} c_f^{(1)}(R). \tag{63}$$

Fig. 23(a) shows that the simulation results are in agreement with the asymptotic relation (63). The leading term $c_f^{(0)}(R)$ from extrapolation to $Ha \to \infty$ is shown in

Fig. 23(b) for the four different values of R in the simulations. For comparison, the friction coefficients from the friction law (57) with $N_c = 0.6$ are shown as Harris' approximation, and further extrapolated results are shown from the mixing-length models of Lykoudis & Brouillette (L&B) [72] and Alboussière & Lingwood (A&L) [15]. Remarkably, the simple closure leading to (57) provides better agreement with the extrapolated data than the more involved models.

5.4 Channel flow with uniform spanwise magnetic field

5.4.1 Subcritical transition [11]

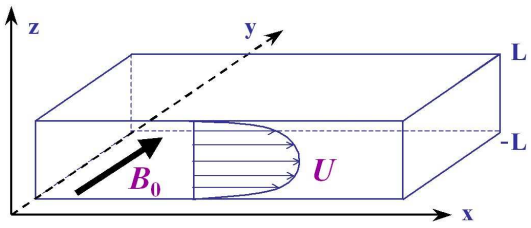

Figure 24: *Sketch of channel flow with spanwise magnetic field. The directions x and y are periodic.*

Channel flow with spanwise magnetic field is the counterpart to Hartmann flow as an idealization of MHD flow in a rectangular duct. Its geometry is shown schematically in Fig. 24. It is obtained by replacing the distant walls perpendicular to the magnetic field with periodic boundary conditions. For Hartmann flow, the distant walls are parallel to the magnetic field. The investigation of transition and turbulence in channel flows with spanwise magnetic field is therefore of comparable interest as in the Hartmann flow. It is also motivated by the same applications.

In contrast to the Hartmann flow the magnetic field produces no Lorentz force on the mean flow when it is oriented in the spanwise direction, i.e. the term $\sigma B^2 (u - U_{\mathrm{av}})$ is missing in the averaged streamwise momentum equation (43). The laminar solution is therefore the parabolic Poiseuille flow, and there is no modification of the shear length scale as in the Hartmann flow, where a modified Reynolds number R based on the Hartmann layer thickness δ is required. For the flow with spanwise field, the relevant Reynolds number is the same as in the non-magnetic case, i.e. $Re = U_0 L/\nu$ based on the half-channel width L.

Linear instability in non-magnetic channel flow originates from two-dimensional perturbations known as Orr modes, which are independent of the spanwise coordinate. These modes are also unaffected by the magnetic field, i.e. there is no change in the critical Reynolds number $Re_c \approx 5772.2$ for linear instability when Ha is non-zero. However, this invariance of Re_c does not carry over to subcritical transition at $Re < Re_c$. The latter is mediated by three-dimensional perturbations, which experience a Lorentz force under a spanwise magnetic field. The modifications of such

three-dimensional perturbations by the spanwise magnetic field and their secondary instability leading to transition were the subject of a detailed investigation by the author in collaboration with D. Krasnov, M. Rossi and O. Zikanov. The results have been published in [11] and will be summarized below.

Subcritical transition in shear flows can be initiated by linear perturbations with strong transient growth of the perturbation energy due to the lift-up effect. These perturbations typically have the form of streamwise vortices. The lift-up effect produces wall-normal vorticity from wall-normal displacement of fluid parcels which maintain their streamwise velocity. It thereby creates elongated, tubular regions with accelerated or decelerated fluid, which are also know as streamwise streaks. These flow structures are sensitive to secondary perturbations and thereby lead to transition.

The investigation of the transient amplification and the structure of such linear perturbations in the channel flow with spanwise magnetic field requires a suitable numerical code, which is explained in [11]. This code implements a fixed-point iteration with consecutive time integration of the linearized perturbation equations and their adjoint equations. The perturbations are represented as Fourier modes with stream- and spanwise wavenumbers α und β, i.e.

$$(\boldsymbol{v}_p, \phi_p, p_p) = (\hat{u}(z,t), \hat{v}(z,t), \hat{w}(z,t), \hat{\phi}(z,t), \hat{p}(z,t)) \exp(i\alpha x + i\beta y). \tag{64}$$

The result of the fixed-point iteration is the initial condition $\hat{u}(z,0)$, $\hat{v}(z,0)$, $\hat{w}(z,0)$, $\hat{\phi}(z,0)$ und $\hat{p}(z,0)$ providing the largest energy amplification

$$G = \sup_{\text{initial cond.}} \left\{ \frac{E_p(\hat{u}(z,T), \hat{v}(z,T), \hat{w}(z,T), \alpha, \beta)}{E_p(\hat{u}(z,0), \hat{v}(z,0), \hat{w}(z,0), \alpha, \beta)} \right\} \tag{65}$$

for given parameters Re, Ha, wavenumbers α, β and time interval T. The energy functional is simply the kinetic energy

$$E_p = \frac{1}{2} \int \left[|\hat{u}(z,T)|^2 + |\hat{v}(z,T)|^2 + |\hat{w}(z,T)|^2 \right] \mathrm{d}z \tag{66}$$

of the perturbation.

The numerical computations with this linear code have shown that the structure of optimal perturbations changes under the influence of the spanwise magnetic field. The effect is illustrated schematically in Fig. 25. Without magnetic field, the strongest transient growth occurs for streamwise vortices. As the Lorentz force tends to eliminate gradients in the direction of the magnetic field, the energy amplification by such structures is significantly weakened in the presence of the magnetic field. A scaling analysis for $Ha \gg 1$ provides the relation

$$G_{\text{opt}} \sim \frac{Re^2}{Ha^2} \tag{67}$$

for the maximum energy amplification of streamwise optimal modes (vortices) with $\alpha = 0$ and optimal values

$$\beta_{\text{opt}} \sim Ha^{-1}, \quad T_{\text{opt}} \sim Re \tag{68}$$

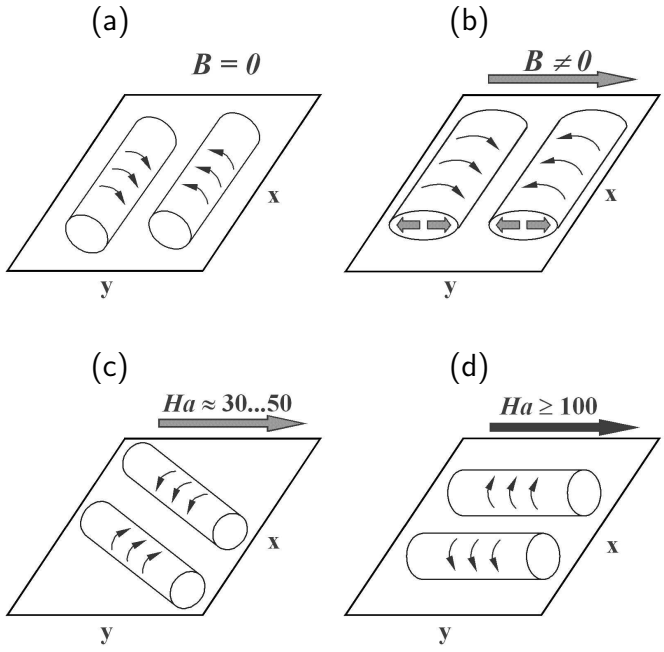

Figure 25: *Schematic representation of the influence of the magnetic field on the orientation of optimal linear perturbations. The mirror image with respect to the plane $y = const.$ provides a symmetric perturbation with identical transient growth.*

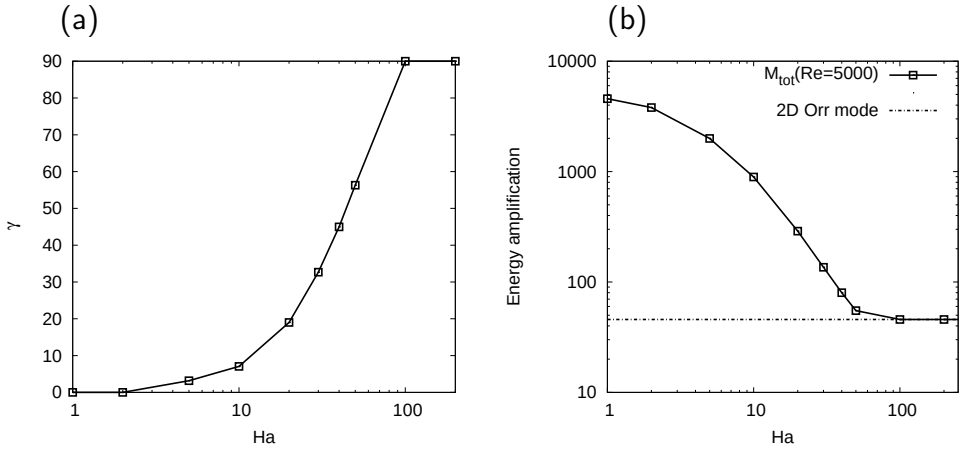

Figure 26: *(a): Tilt angle γ of the axis of the optimal perturbation with respect to the flow direction and (b) maximum energy amplification as functions of Ha for $Re = 5000$. The optimal wavelength changes only slightly with Ha.*

for the spanwise wavenumber and time. The numerical code confirms these scalings and provides the prefactors

$$G_{\rm opt} \approx 0.0018\,\frac{Re^2}{Ha^2}, \quad \beta_{\rm opt} \approx 8.2 Ha^{-1}, \quad T_{\rm opt} \approx 0.037 Re. \tag{69}$$

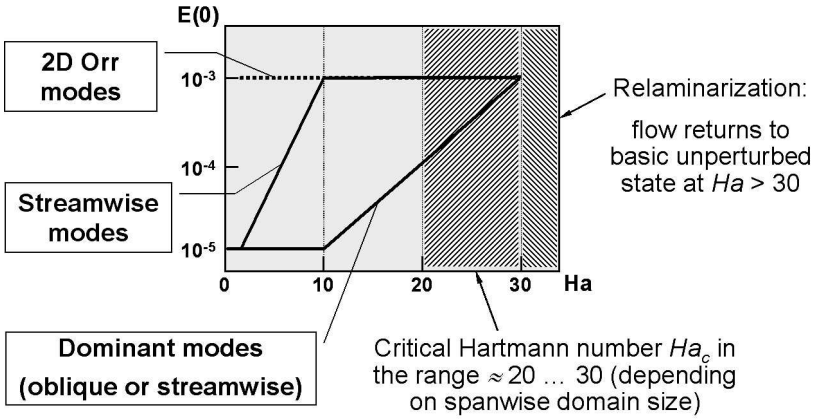

Figure 27: *Schematic representation of results from transition simulations for* $Re = 5000$. *The normalized perturbation energy* $E(0)$ *required for transition is shown for different types of perturbations.* $E(0)$ *is normalized by the kinetic energy of the basic flow.*

The strong damping influence of the Lorentz force can be reduced by tilting of the streamwise modes into the spanwise direction. However, this also weakens the lift-up mechanism because the wall-normal displacement of fluid elements produces less wall-normal vorticity. The interplay of these effects causes the behavior shown in Fig. 26 at $Re = 5000$. For moderate magnetic fields, the strongest transient growth occurs for oblique modes. The tilt angle

$$\gamma = \arctan(\alpha/\beta) \tag{70}$$

increases with the strength of the magnetic field and finally reaches 90 degrees. In this case the lift-up mechanism is inactive, and the Lorentz force is completely absent. Transient growth is only provided by the comparatively weak viscous mechanism of the Orr modes. It is responsible for the plateau of G at large values of Ha in Fig. 26(b).

Secondary instabilities of finite-amplitude optimal perturbations were investigated by direct numerical simulations at $Re = 5000$ and various values of Ha. In order to trigger such instabilities, the direct simulations were started either with linear combinations of symmetric oblique modes with the same α and either β or $-\beta$, or with a pure optimal mode with spatially random noise added at the time of maximum energy amplification. The simulations show that oblique modes are most efficient in destabilizing the flow for values $5 \lesssim Ha \lesssim 30$, and that interacting symmetric oblique modes provide a plausible transition scenario. For larger values of Ha the transition could not be triggered at realistic perturbations amplitudes. The basic flow remains stable in this case. These results are schematically summarized in Fig. 27.

5.4.2 Direct and large eddy simulations of turbulent drag reduction [12, 13]

The laminar flow is unstable for Reynolds numbers $Re > Re_c$. As a consequence, the flow attains a state of developed turbulence also for weak or moderate magnetic fields. The properties of the turbulent state increasingly deviate from the hydrodynamic case when the Hartmann number is raised. These changes were investigated in a parametric study by D. Krasnov, O. Zikanov and J. Schumacher in collaboration with the author. Our results from direct numerical simulations and large eddy simulations are documented in the papers [12, 13].

The main effect of the magnetic field is a reduction of the friction drag. The magnetic damping strongly affects flow structures with rapid spatial variation along the field direction. For the spanwise orientation these are precisely the structures involved in near-wall production of turbulence such as slow-speed streaks and hairpin vortices. The spanwise magnetic field can therefore lead to significant drag reduction in spite of the additional Joule dissipation. Turbulent drag reduction in this configuration was already noted in the experiments by Hartmann and Lazarus with elongated ducts, although the interaction of the field with the mean flow eventually leads to drag increase with Ha on account of the Hartmann walls perpendicular to the magnetic field [102].

Direct numerical simulations of turbulent channel flow with spanwise magnetic field were performed by Lee & Choi [65] at the subcritical Reynolds number $Re = 3000$. They observed drag reduction and eventual relaminarization of the flow. The present parametric study goes considerbly further in terms of Reynolds numbers and in the level of analysis, especially with regard to the energy dissipation discussed in [13]. The extensive parallel computations were again largely performed with a grant of computing time from the von Neumann Institute for Computing in Jülich.

Two Reynolds numbers $Re = 10^4$ and $Re = 2 \times 10^4$ are considered for the aspect ratio $2\pi L \times \pi L \times 2L$ in [12, 13]. The friction coefficient c_f decreases by about 30% when Ha is increased from $Ha = 0$ to $Ha = 30$ for $Re = 10^4$ and to $Ha = 40$ for $Re = 2 \times 10^4$. For larger Ha one finds the large-scale intermittency, which will be described below. The drag reduction by 30% is considerable, but the laminar flow has a friction coefficient that is ten times smaller than for the turbulent state at $Ha = 0$.

The drag reduction is associated with a modification of the mean velocity profile in Fig. 28. The slope near the wall is reduced with Ha, and the profile becomes steeper in the middle of the channel. For the larger values of Ha the profile has a certain resemblance with the laminar profile. In the semi-logarithmic representation (Fig. 28(b)) one can see that u^+ deviates increasingly from the logarithmic law of the wall for hydrodynamic channel flow. This was already suggested for the low Reynolds number $Re \approx 3000$ in [65], but could only be unambiguously confirmed in the present study. The drag reduction and modification of the velocity profile by the spanwise magnetic field are manifestly different from those in polymer solutions, where the logarithmic dependence on z^+ is preserved [17]. They are comparable with those in channel flow with density stratification, which have been obtained by large

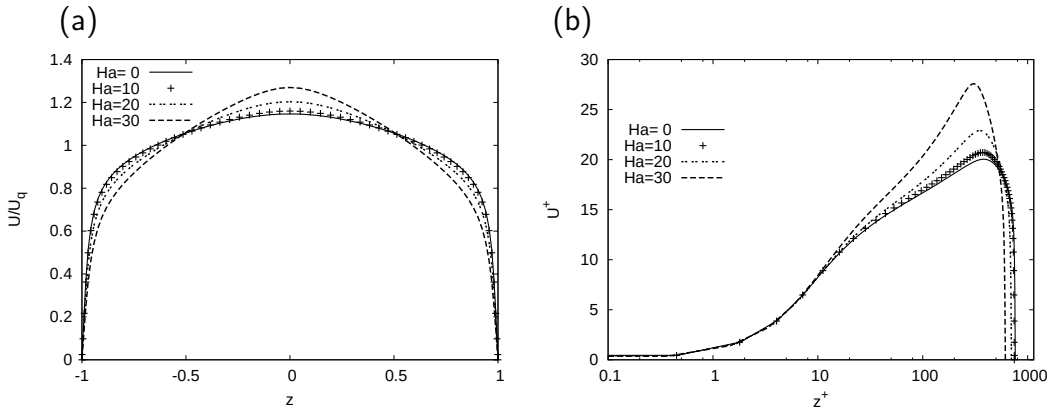

Figure 28: *Mean velocity profiles for $Re = 10^4$ and different Ha: (a) normalized by the mean velocity U_q; (b) normalized by the friction velocity u_τ and the friction length ν/u_τ.*

eddy simulations [16].

The explanation for the disappearance of the logarithmic dependence on z^+ remains an open problem. The average streamwise momentum equation (43) has no Lorentz force term, i.e. the magnetic damping is exclusively in the Reynolds stress term. As a consequence, there is no obvious reason why the usual arguments leading to the logarithmic law of the wall fail in the case of spanwise magnetic field. More speculation on this issue can be found in [12].

Another aspect of the study in [12, 13] is the validation of large eddy simulations by comparison with direct simulations. Two common closures for the subgrid stresses are considered, namely the classical Smagorinsky model and the Smagorinsky model with the dynamic procedure suggested by Germano et al. [41] and improved by Lilly [68]. The classical Smagorinsky model is used in the version adapted to hydrodynamic channel flows [75]. The so-called dynamic model is used with test filtering in the periodic streamwise and spanwise directions. The simulation results show that the classical Smagorinsky model cannot reproduce the modification of the flow by the spanwise field with acceptable accuracy. By contrast, the dynamic model provides good agreement for all values of Ha considered. This finding is in line with the general observation that the dynamic model adapts effectively to spatial variations in the large scales, e.g. in wall-bounded or transitional flows [40].

5.4.3 Large-scale intermittency [14]

Further numerical work on this problem explored the behavior at supercritical Re for moderately strong magnetic fields. It is documented in the joint publication [14] by the author together with D. Krasnov, A. Thess and O.Zikanov. Turbulence will not be sustained in this case because of the significant Joule dissipation, i.e. the flow should evolve towards the laminar state. On the other hand, the laminar state

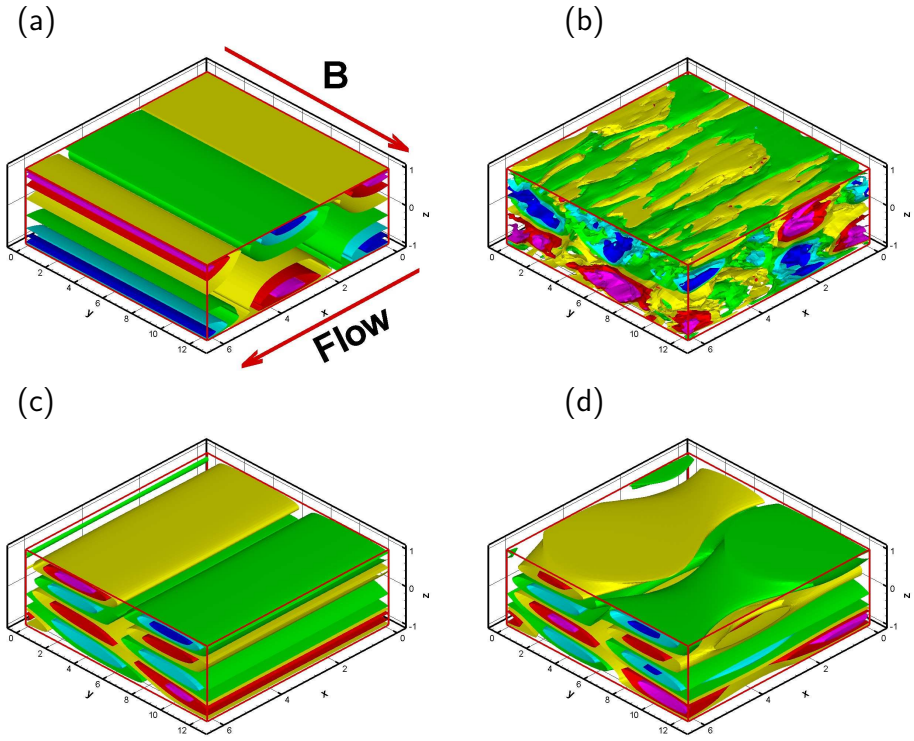

Figure 29: *Flow evolution during one cycle of the intermittent process. Four stages are shown using isosurfaces of streamwise velocity perturbations normalized by corresponding rms values. (a) growing two-dimensional spanwise TS mode, (b) turbulent state at the maximum of perturbation energy, (c) decaying flow dominated by streamwise streaks, (d) disappearance of the streamwise streaks and return of the growing TS waves.*

is unstable. At least one Orr mode has a positive growth rate above Re_c, and is unaffected by the magnetic field. As a result one observes an intermittent dynamics, which is characterized by several stages. They are illustrated in Fig. 29, which shows snapshots of the streamwise velocity perturbation from a simulation with $Re = 8000$ and $Ha = 80$. The corresponding evolution of the driving pressure gradient is shown in Fig. 30.

In the first stage, the flow is initially close to the laminar state. It departs from this state by exponential growth of an unstable Orr mode, which is marked as (a) in Fig 29. Alternatively, this mode is called Tollmien-Schlichting (TS) mode in [14]. After some time, this Orr/TS mode reaches an amplitude where secondary instabilities become amplified, and transition takes place (b). The resulting turbulent state is immediately suppressed, i.e. the flow decays towards the laminar state (c). This decay stage ends when the flow approaches the laminar state, where the unstable Orr mode is again seeded by the fluctuating background, which is either due to the inherent numerical "noise" from finite-precision arithmetic, or due to an explicit noise term (stage d).

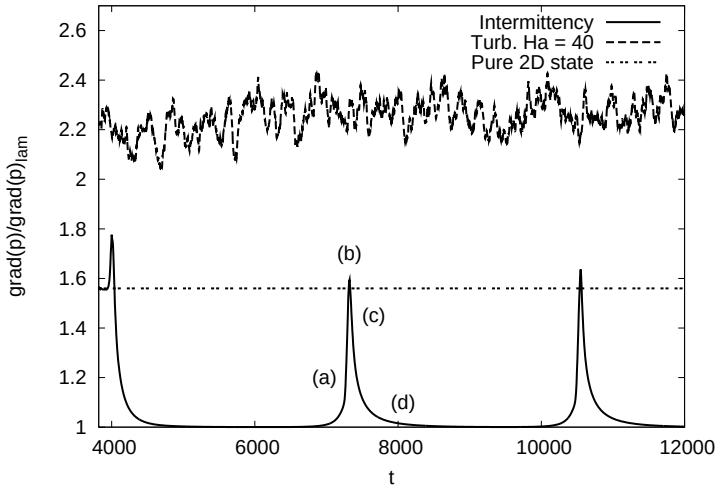

Figure 30: *Mean pressure gradient (normalized to the basic flow) at* $Re = 8000$ *for the intermittent state at* $Ha = 80$*, for purely two-dimensional channel flow [52], and for fully developed turbulence at* $Ha = 40$*.*

After that, the cycle repeats itself.

During the intermittency cycle, the friction coefficient c_f (and thereby the driving pressure gradient) remains close to the laminar value except for the short interval corresponding to the turbulent "burst". Remarkably, c_f is not only lower than for sustained turbulent flow realized at weaker magnetic fields. Except for the short bursts, c_f is also lower than for the time-dependent, purely two-dimensional flow investigated by Jimenez [52]. At the parameters studied in [14], this two-dimensional solution is a traveling wave state, which is unaffected by the magnetic field.

In the simulations of channel flow with spanwise magnetic field the intermittent solution appears to be a robust phenomenon. It is found for both computational domains considered, which differ in their streamwise periodicity length, and over a significant interval of Hartmann numbers for a given, supercritical Reynolds number. In the configuration shown in Figs. 29,30 the intermittent solution is only suppressed when the Hartmann number exceeds $Ha \approx 200$.

From a more general viewpoint, the intermittent dynamics in channel flow with spanwise field presents another realization of an apparently generic intermittency phenomenon in MHD flows with interaction parameters of order unity. Previous observations of such intermittent solutions were made in numerical simulations of forced, homogeneous MHD turbulence in a periodic box [108] and for inviscid flow in a tri-axial ellipsoid with the magnetic field aligned with one axis [99]. In comparison with these cases, the channel flow is considerably more realisitic because it incorporates the effects of solid walls, viscosity and mean shear. On the other hand, it is still a considerable simplification of experimental reality because of the missing lateral channel walls and the periodicity in streamwise direction. More realistic simulations

in the duct geometry, i.e. including lateral walls, are a possible next step towards an eventual experimental verification of intermittency in wall-bounded MHD flows. This aspect and further open issues in the channel simulations are also discussed in [14].

5.5 Summary

Experiments on transition and turbulence in wall-bounded magnetohydrodynamic flows can only provide very limited information because liquid metal flows preclude optical flow measurements. Accurate numerical simulations become therefore particularly important. The works presented in this section are focused on the channel geometry, i.e. they have neglected the influence of lateral walls. The publication [10] presents the first systematic study of the mean properties of turbulent Hartmann flow. The publications [11, 12, 13, 14] are concerned with the case of spanwise magnetic field and address transition and turbulence comprehensively. The publication [11] is the first systematic numerical transition study for the configuration with spanwise field. The properties of the turbulent state are addressed in [12, 13], which provide a more detailed picture than the previous study [65] at subcritical Reynolds number. In addition, the utility of the dynamic Smagorinsky model for wall-bounded magnetohydrodynamic flows has been demonstrated in [12] on the basis of DNS results.

Large-scale intermittency as found in [14] could have a significant impact on conventional views of turbulence suppression by magnetic fields, provided it can be realized in the presence of side walls.

6 Conclusions

Nature and technology abound with fluid flows on a wide range of length and time scales and under the influence of various forces. The focus of the works summarized above is on some of the effects associated with shear, interfacial tension, buoyancy, and electromagnetic forces. A common aspect is the fairly simple geometry of the fluid domain, whereby one can employ specialized and highly efficient numerical methods. It is typically composed of one or two plane layers.

On the subject of Bénard-Marangoni convection, the author is presently interested in the properties of three-dimensional convection in the limit of zero Prandtl number $Pr = 0$, and in the differences to the case of finite Prandtl number. Preliminary simulation results for $Pr = 0$ are markedly different in the Reynolds number scaling with the Marangoni number. Statistical properties of velocity and temperature fields are another aspect of turbulent Bénard-Marangoni convection that has so far not been discussed in [2].

Instabilities in two-phase shear layers emanating from a nozzle grow with the downstream distance, and should therefore be treated in the framework of spatial stability [51, 33] rather than in that of temporal stability as in [7, 8]. Such analyses have recently appeared for the inviscid case, e.g. [53, 54]. Viscous studies of spatial growth are currently performed by the Ph.D. student Thomas Otto under the supervision of the author and in collaboration with Dr. M. Rossi (University Paris VI). Preliminary results have been published in conference proceedings [80, 81]. The collaboration with Prof. Zaleski (University Paris VI) will resume for studies of the nonlinear development of spatial modes.

On the topic of magnetohydrodynamic flows the author continues the collaboration with Dr. D. Krasnov, who has been a member of the Emmy-Noether junior research group headed by the author. Our current interest is the transition in the magnetohydrodynamic duct flow with lateral walls and uniform magnetic field. For these studies, new finite difference codes for the optimal linear perturbations and for fully nonlinear simulations (DNS) have been developed mostly by Dr. Krasnov. Our collaborators on this topic are Prof. Zikanov (University of Michigan-Dearborn) and Dr. M. Rossi. A joint grant proposal with Prof. A. Thess for further numerical and experimental investigation of the large-scale intermittency in an annular duct with axial magnetic field was submitted to the Deutsche Forschungsgemeinschaft in 2008. It is currently under review. In the framework of the research training group (Graduiertenkolleg) "Lorentz Force Velocimetry and Lorentz Force Eddy Current Testing" the author is jointly responsible with Prof. Schumacher and Prof. Thess for two projects on the interactions of localized magnetic fields with liquid metal flows. This work will commence in January 2010.

A Appendix: Quasistatic approximation

The motion of a conducting liquid in a magnetic field $\boldsymbol{B}$ gives rise to an induced current density $\boldsymbol{j}$, which produces a Lorentz force density $\boldsymbol{j} \times \boldsymbol{B}$ acting on the flow. The fluid remains electrically neutral because of its high conductivity, i.e. the induced currents are solenoidal. The induced currents also modify the magnetic field because of Ampère's law. Displacement currents are neglected in Ampère's law.

The equations describing the electric and magnetic fields in the conducting fluid are

$$\begin{aligned} \nabla \cdot \boldsymbol{B} &= 0 && (71)\\ \nabla \cdot \boldsymbol{j} &= 0 \quad \text{(charge conservation)} && (72)\\ \mu_0 \boldsymbol{j} &= \nabla \times \boldsymbol{B} \quad \text{(Ampère's law)} && (73)\\ -\frac{\partial \boldsymbol{B}}{\partial t} &= \nabla \times \boldsymbol{E} \quad \text{(Faraday's law)} && (74)\\ \boldsymbol{j} &= \sigma \left(\boldsymbol{E} + \boldsymbol{v} \times \boldsymbol{B} \right), \quad \text{(Ohm's law)} && (75) \end{aligned}$$

The induction equation is obtained in two steps. First, Ohm's law is solved for the electric field, and the resulting expression substituted into Faraday's law. After that, the current density is expressed by Ampère's law. The result is

$$\frac{\partial \boldsymbol{B}}{\partial t} = \eta \nabla^2 \boldsymbol{B} + \nabla \times \left(\boldsymbol{v} \times \boldsymbol{B} \right), \tag{76}$$

where $\nabla \cdot \boldsymbol{B} = 0$ has been used. The quantity

$$\eta = \frac{1}{\sigma \mu_0} \tag{77}$$

is the magnetic diffusivity of the conducting liquid. It is of the order 1 m^2/s for typical liquid metals, i.e. about 10^6 times larger than the typical kinematic viscosity.

To simplify the induction equation for the typical applications of liquid-metal magnetohydrodynamics one now introduces nondimensional quantities on the basis of the scales L, U and L/U for length, velocity and time, which are characteristic of the fluid flow. The scale of the magnetic field is B_0, which is typical of the imposed magnetic field in absence of fluid flow. The nondimensional form of the induction equation then becomes

$$R_m \frac{\partial \tilde{\boldsymbol{B}}}{\partial \tilde{t}} = \tilde{\nabla}^2 \tilde{\boldsymbol{B}} + R_m \tilde{\nabla} \times \left(\tilde{\boldsymbol{v}} \times \tilde{\boldsymbol{B}} \right), \tag{78}$$

where the tilde indicates the dimensionless quantities and

$$R_m = \sigma \mu_0 U L \tag{79}$$

is the magnetic Reynolds number, which is typically small compared with unity for velocities and lengthscales of laboratory and industrial flows. One can therefore consider R_m as a small quantity ϵ and try a regular perturbation expansion

$$\boldsymbol{B} = \sum_{n=0}^{\infty} \epsilon^n \boldsymbol{B}^{(n)} \tag{80}$$

for the solution of the induction equation, which is then placed into the dimensionless induction equation. Omitting the tilde for ease of notation, one obtains

$$\nabla^2 \boldsymbol{B}^{(0)} = 0 \tag{81}$$

at order ϵ^0 and

$$\frac{\partial}{\partial t}\boldsymbol{B}^{(0)} = \nabla^2 \boldsymbol{B}^{(1)} + \nabla \times \left(\boldsymbol{v} \times \boldsymbol{B}^{(0)}\right) \tag{82}$$

at order ϵ^1. The leading term in the magnetic field represents the imposed magnetic field produced outside the liquid. The next term provides the first-order response in the magnetic field to the presence of the moving fluid. Higher-order contributions are not considered because $\epsilon = R_m$ is assumed to be small. The currents and electric fields induced in the fluid can also be written as expansions in ϵ with leading term ϵ^1. The unit for the electric current density $\boldsymbol{j}$ is chosen as $B_0/\mu_0 L$ and the unit for the electric field $\boldsymbol{E}$ is chosen as and $B_0/\sigma\mu_0 L$. Placing the expansions into Ampère's and Ohm's laws one finds

$$\boldsymbol{j}^{(n)} = \nabla \times \boldsymbol{B}^{(n)} \tag{83}$$

$$\boldsymbol{j}^{(n)} = \boldsymbol{E}^{(n)} + \boldsymbol{v} \times \boldsymbol{B}^{(n-1)}, \tag{84}$$

whereby it follows that

$$\nabla \times \boldsymbol{B}^{(n)} = \boldsymbol{E}^{(n)} + \boldsymbol{v} \times \boldsymbol{B}^{(n-1)}. \tag{85}$$

At order ϵ^1 one finds by taking the curl of equation (85) that

$$\nabla \times \boldsymbol{E}^{(1)} = -\nabla^2 \boldsymbol{B}^{(1)} - \nabla \times \left(\boldsymbol{v} \times \boldsymbol{B}^{(0)}\right) = -\frac{\partial}{\partial t}\boldsymbol{B}^{(0)}. \tag{86}$$

The curl of the electric field at this order of approximation is therefore zero provided that the imposed magnetic field is time-independent. One can therefore write the electric field as a gradient, i.e.

$$\boldsymbol{E}^{(1)} = -\nabla \Phi^{(1)}. \tag{87}$$

For a time-independent imposed external field $\boldsymbol{B}^{(0)}$, the first-order approximation for the induced currents can be represented by a magnetic field perturbation $\boldsymbol{B}^{(1)}$ as

$$\boldsymbol{j}^{(1)} = \nabla \times \boldsymbol{B}^{(1)}, \tag{88}$$

$$\nabla^2 \boldsymbol{B}^{(1)} = -\nabla \times \left(\boldsymbol{v} \times \boldsymbol{B}^{(0)}\right). \tag{89}$$

The equivalent representation using the electric potential is

$$\begin{aligned} \boldsymbol{j}^{(1)} &= -\nabla\Phi^{(1)} + \boldsymbol{v} \times \boldsymbol{B}^{(0)}, && (90) \\ \nabla \cdot \boldsymbol{j}^{(1)} &= 0. && (91) \end{aligned}$$

The condition (91) is needed to ensure that the currents are solenoidal in agreement with equation (72). It determines the electric potential as solution of the Poisson equation

$$\nabla^2\Phi^{(1)} = \nabla \cdot \left(\boldsymbol{v} \times \boldsymbol{B}^{(0)} \right). \tag{92}$$

The nondimensional Lorentz force is given by the expression

$$\boldsymbol{f}^{(1)} = \boldsymbol{j}^{(1)} \times \boldsymbol{B}^{(0)} \tag{93}$$

to first order approximation.

B References

15. T. Alboussière and R. J. Lingwood. A model for the turbulent Hartmann layer. *Phys. Fluids*, 12:1535–43, 2000.

16. V. Armenio and S. Sarkar. An investigation of stably stratified turbulent channel flow using large-eddy simulation. *J. Fluid Mech.*, 459:1, 2002.

17. R. Benzi, E. De Angelis, V. S. L'vov, I. Procaccia, and V. Tiberkevich. Maximum drag reduction asymptotes and the cross-over to the Newtonian plug. *J. Fluid Mech.*, 551:185, 2006.

18. M. J. Block. Surface tension as the cause of Bénard cells and surface deformation in a liquid film. *Nature*, 178:650–651, 1956.

19. T. Boeck. *Bénard-Marangoni convection at low Prandtl numbers - Results of direct numerical simulations*. Doctoral thesis, TU Ilmenau, 2000.

20. T. Boeck, J. Li, E. Lopez-Pages, P. Yecko, and S.Zaleski. Ligament formation in sheared liquid-gas layers. *Theoretical and Computational Fluid Dynamics*, 21:59–76, 2007.

21. T. Boeck and A. Thess. Inertial Bénard-Marangoni convection. *J. Fluid Mech.*, 350:149–175, 1997.

22. T. Boeck and A. Thess. Turbulent Bénard-Marangoni convection: Results of two-dimensional simulations. *Phys. Rev. Lett.*, 80:1216–1219, 1998.

23. T. Boeck and A. Thess. Bénard-Marangoni convection at low Prandtl number. *J. Fluid Mech.*, 399:251–275, 1999.

24. T. Boeck and A. Thess. Direct numerical simulation of Marangoni convection in a two-fluid system. In F. Keil, W. Mackens, H. Voß, and J. Werther, editors, *Scientific Computing in Chemical Engineering II*, pages 352–359. Springer, 1999.

25. H. Branover. *Magnetohydrodynamic Flow in Ducts*. John Wiley, New York, 1978.

26. L. M. Braverman, K. Eckert, A. A. Nepomnyashchy, I. B. Simanovskii, and A. Thess. Convection in two-layer systems with an anomalous thermocapillary effect. *Phys. Rev. E*, 62:3619–3631, 2000.

27. L. Bühler. Liquid metal magnetohydrodynamics for fusion blankets. In S. Molokov, R. Moreau, and H. K. Moffatt, editors, *Magnetohydrodynamics: Historical Evolution and Trends*, pages 171–194. Springer, 2007.

28. S. Chandrasekhar. *Hydrodynamic and Hydromagnetic Stability*. Oxford University Press, 1961.

29. G. P. Chini. Strongly nonlinear Langmuir circulation and Rayleigh-Bénard convection. *J. Fluid Mech.*, 614:39–65, 2009.

30. T. Clune and E. Knobloch. Pattern selection in three-dimensional magnetoconvection. *Physica D*, 74:151–176, 1994.

31. P. Colinet, J. C. Legros, and M. G. Velarde. *Nonlinear Dynamics of Surface-Tension-Driven Instabilities*. Wiley-VCH, 2001.

32. A. V. Coward, Y. Y. Renardy, M. Renardy, and J. R. Richards. Temporal Evolution of Periodic Disturbances in Two-Layer Couette Flow. *J. Comput. Phys.*, 132:346–361, 1997.

33. W. O. Criminale, T. L. Jackson, and R. D. Joslin. *Theory and Computation of Hydrodynamic Stability*. Cambridge University Press, Cambridge, 2003.

34. P. A. Davidson. Magnetohydrodynamics in materials processing. *Annu. Rev. Fluid Mech.*, 31:273–300, 1999.

35. P. A. Davidson. *An Introduction to Magnetohydrodynamics*. Cambridge University Press, 2001.

36. T. DebRoy and S. A. David. Physical processes in fusion welding. *Rev. Mod. Phys.*, 67:85–112, 1995.

37. C. R. Doering. private communication, 2008.

38. P. G. Drazin. *Introduction to Hydrodynamic Stability*. Cambridge University Press, 2002.

39. J. Eggers. Nonlinear dynamics and breakup of free-surface flows. *Rev. Mod. Phys.*, 69:865–929, 1997.

40. J. Fröhlich. *Large Eddy Simulation turbulenter Strömungen*. Teubner Verlag, 2006.

41. M. Germano, U. Piomelli, P. Moin, and W. H. Cabot. A dynamic subgrid-scale eddy viscosity model. *Phys. Fluids*, 3(7):1760–1765, 1991.

42. M. Ghorokhovski and M. Herrmann. Modelling primary atomization. *Annu. Rev. Fluid Mech.*, 40:343–366, 2008.

43. J. M. Gordillo, M. Pérez-Saborid, and A. M. Ganán-Calvo. Linear stability of co-flowing liquid-gas jets. *J. Fluid Mech.*, 448:23–51, 2001.

44. D. Gueyffier, A. Nadim, J. Li, R. Scardovelli, and S. Zaleski. Volume of Fluid interface tracking with smoothed surface stress methods for three-dimensional flows. *J. Comput. Phys.*, 152:423–456, 1999.

45. L. P. Harris. *Hydromagnetic Channel Flows*. M.I.T. Press and John Wiley, New York, 1960.

46. J. Hartmann. Hg-dynamics I: Theory of the laminar flow of an electrically conductive liquid in a homogeneous magnetic field. *K. Dan. Vidensk. Selsk. Mat. Fys. Medd.*, 15(6):1–28, 1937.

47. J. Hartmann and F. Lazarus. Hg-dynamics II: Experimental investigations on the flow of mercury in a homogeneous magnetic field. *K. Dan. Vidensk. Selsk. Mat. Fys. Medd.*, 15(7):1–45, 1937.

48. E.J. Hinch. A note on the mechanism of the instability at the interface between two shearing fluids. *J. Fluid Mech.*, 144:463–465, 1984.

49. G. M. Homsy. *Multimedia fluid mechanics*. Cambridge, 2nd edition, 2008.

50. A. P. Hooper and W. G. C. Boyd. Shear-flow instability at the interface between two viscous fluids. *J. Fluid Mech.*, 128:507–528, 1983.

51. P. Huerre and M. Rossi. Hydrodynamic instabilities in open flows. In C. Godrèche and P. Manneville, editors, *Hydrodynamics and Nonlinear Instabilities*, Collection Aléa Saclay, pages 81–288. Cambridge University Press, 1998.

52. J. Jimenez. Transition to turbulence in two-dimensional Poiseuille flow. *J. Fluid Mech.*, 218:265–297, 1990.

53. M. P. Juniper. The effect of confinement on the stability of two-dimensional shear flows. *J. Fluid Mech.*, 565:171–195, 2006.

54. M. P. Juniper and S. Clandel. The stability of ducted compound flows and consequences for the geometry of coaxial injectors. *J. Fluid Mech.*, 482:257–269, 2003.

55. S. Kenjerec and A. Hanjalic. On the implementation of effects of Lorentz force in turbulence closure models. *Int. J. of Heat and Fluid Flow*, 21:329–337, 2000.

56. B. Knaepen, S. Kassinos, and D. Carati. Magnetohydrodynamic turbulence at moderate magnetic Reynolds number. *J. Fluid Mech.*, 513:199–220, 2004.

57. B. Knaepen and P. Moin. Large-eddy simulation of conductive flows at low magnetic Reynolds number. *Phys. Fluids*, 16:1255–1261, 2004.

58. B. Knaepen and R. Moreau. Magnetohydrodynamic turbulence at low magnetic Reynolds number. *Annu. Rev. Fluid Mech.*, 40:25–45, 2008.

59. H. Kobayashi. Large eddy simulation of magnetohydrodynamic turbulent channel flows with local subgrid-scale model based on coherent structures. *Phys. Fluids*, 18:045107, 2006.

60. D. Krasnov, E. Zienicke, O. Zikanov, T. Boeck, and A. Thess. Numerical study of the instability of the Hartmann layer. *J. Fluid Mech.*, 504:183–211, 2004.

61. H. C. Kuhlmann. *Thermocapillary convection in models of crystal growth*. Springer, 1999.

62. B. Lafaurie, C. Nardone, R. Scardovelli, S. Zaleski, and G. Zanetti. Modelling merging and fragmentation in multiphase flows with SURFER. *J. Comput. Phys.*, 113:134–147, 1994.

63. L.D. Landau and E.M. Lifshitz. *Fluid Mechanics*. Pergamon, 2nd edition, 1987.

64. J. C. Lasheras and E. J. Hopfinger. Liquid jet instability and atomization in a coaxial gas stream. *Annu. Rev. Fluid Mech.*, 32:275–308, 2000.

65. D. Lee and H. Choi. Magnetohydrodynamic turbulent flow in a channel at low magnetic Reynolds number. *J. Fluid Mech.*, 429:367–394, 2001.

66. A. H. Lefebvre. *Atomization and Sprays*. Taylor & Francis, 1989.

67. X. Li and R. S. Tankin. On the temporal instability of a two-dimensional viscous liquid sheet. *J. Fluid Mech.*, 226:425–443, 1991.

68. D. K. Lilly. A proposed modification to the Germano subgrid-scale closure model. *Phys. Fluids*, 4:633, 1992.

69. S. P. Lin and R. D. Reitz. Drop and spray formation from a liquid jet. *Annu. Rev. Fluid Mech.*, 30:85–105, 1998.

70. R. J. Lingwood and T. Alboussière. On the stability of the Hartmann layer. *Phys. Fluids*, 11:2058–2068, 1999.

71. R. C. Lock. The velocity distribution in the laminar boundary layer between parallel streams. *Q. J. Mech. Appl. Math.*, 4:42–63, 1951.

72. P. S. Lykoudis and E. C. Brouillette. Magneto-Fluid-Mechanic Channel Flow. II. Theory. *Phys. Fluids*, 10(5):1002–1007, 1967.

73. P. Marmottant and E. Villermaux. On spray formation. *J. Fluid Mech.*, 498:73–111, 2004.

74. J. Marra and J. A. M. Huethorst. Physical principles of Marangoni drying. *Langmuir*, 7:2748–2755, 1991.

75. P. Moin and J. Kim. Numerical investigation of turbulent channel flow. *J. Fluid Mech.*, 118:341–377, 1982.

76. P. Moresco and T. Alboussière. Experimental study of the instability of the Hartmann layer. *J. Fluid Mech.*, 504:167–181, 2004.

77. W. Murgatroyd. Experiments on magnetohydrodynamic channel flow. *Philos. Mag.*, 44:1348–1354, 1953.

78. A. Nepomnyashchy, I. Simanovskii, and J. C. Legros. *Interfacial Convection in Multilayer Systems*. Springer, 2006.

79. R. R. Nourgaliev, M. S. Liou, and T. G. Theofanous. Numerical prediction of interfacial instabilities: Sharp interface method. *J. Comp. Phys.*, 227:3940–3970, 2008.

80. T. Otto, M. Rossi, and T. Boeck. Spatial instability of two-phase mixing layers. In *Proceedings of the 22nd European Conference on Liquid Atomization and Spray Systems*, Como Lake, Italy, 2008.

81. T. Otto, M. Rossi, and T. Boeck. Spatial instability of two-phase mixing layers. *Proc. Appl. Math. Mech.*, 8:10635–10636, 2008.

82. S. V. Patankar. *Numerical Heat Transfer and Fluid Flow*. Taylor & Francis, 1980.

83. J. R. A. Pearson. On convection cells induced by surface tension. *J. Fluid Mech.*, 4:489–500, 1958.

84. A. Pumir and L. Blumenfeld. Heat transport in a liquid layer locally heated on its free surface. *Phys. Rev. E*, 54(5):R4528–R4531, 1996.

85. F. Ben Rayana. *Étude des instabilités interfaciales liquide-gaz en atomisation assistée et tailles de gouttes*. PhD thesis, Institut National Polytechnique de Grenoble, 2007.

86. Lord Rayleigh. On convection currents in a horizontal layer of fluid when the higher temperature is on the under side. *Phil. Mag.*, 32:529–546, 1916.

87. J. R. Ristorcelli and J. L. Lumley. Instabilities, transition and turbulence in the Czochralski crystal melt. *J. Crystal Growth*, 116:447–460, 1992.

88. P. G. Saffman. On the spectrum and decay of random two-dimensional vorticity distributions at large Reynolds numbers. *Stud. Appl. Maths*, 50(4):377–383, 1971.

89. S. Satake, T. Kunugi, K. Takase, and Y. Ose. Direct numerical simulation of turbulent channel flow under a uniform magnetic field for large-scale structures at high Reynolds number. *Phys. Fluids*, 18(12):125106, 2006.

90. S. Schiller, U. Heisig, and S. Panzer. *Electron Beam Technology*. Wiley, New York, 1979.

91. P. J. Schmid and D. S. Henningson. *Stability and Transition in Shear Flows*. Springer Verlag, 2001.

92. B. I. Shraiman and E. D. Siggia. Heat transport in high-Rayleigh-number convection. *Phys. Rev. A*, 42:3650–3653, 1990.

93. K. A. Smith. On convective instability induced by surface-tension gradients. *J. Fluid Mech.*, 24:401–414, 1966.

94. M. Sussman, K. M. Smith, M.Y. Hussaini, M. Ohta, and R. Zhi-Wei. A sharp interface method for incompressible two-phase flows. *J. Comput. Phys.*, 221:469–505, 2007.

95. M. Takashima. The stability of the modified plane Poiseuille flow in the presence of a transverse magnetic field. *Fluid Dynamics Research*, 17:293–310, 1996.

96. A. Thess and M. Bestehorn. Planform selection in Bénard-Marangoni convection: l hexagons versus g hexagons. *Phys. Rev. E*, 52(6):6358–6367, 1995.

97. A. Thess and K. Nitschke. On Bénard-Marangoni convection in the presence of a magnetic field. *Phys. Fluids*, 7(5):1176–1178, 1995.

98. A. Thess and S. A. Orszag. Surface-tension-driven Bénard convection at infinite Prandtl number. *J. Fluid Mech.*, 283:201–230, 1995.

99. A. Thess and O. Zikanov. Transition from two-dimensional to three-dimensional MHD turbulence. *J. Fluid Mech.*, 579:383–412, 2007.

100. B. G. Thomas and L. Zhang. Mathematical modeling of fluid flow in continuous casting: a review. *ISIJ Intern*, 41(10):1181–1193, 2001.

101. G. Tryggvason, M. Sussman, and M. Y. Hussaini. Immersed boundary methods for fluid interfaces. In A. Prosperetti and G. Tryggvason, editors, *Computational Methods for Multiphase Flow*, pages 37–77. Cambridge, 2007.

102. A. Tsinober. MHD flow drag reduction. In D.M. Bushnell and J.N. Hefner, editors, *Viscous drag reduction in boundary layers*, pages 327–349, 1990.

103. E. Villermaux. Mixing and spray formation in coaxial jets. *J. Propulsion and Power*, 14:807–817, 1998.

104. W. von Ammon, Yu. Gelfgat, L. Gorbunov, A. Muhlbauer, A. Muiznieks, Y. Makarov, J. Virbulis, and G. Muller. Application of magnetic fields in industrial growth of silicon single crystals. In *The 15^{th} Riga and 6^{th} PAMIR Conference on Fundamental and Applied MHD Modeling of MHD turbulence*, volume I, pages 41–54, Riga, Latvia, 2005.

105. P. Welander. Convective instability in a two-layer fluid heated from above. *Tellus*, XVI:349–358, 1964.

106. S. K. Wilson. The effect of a uniform magnetic field on the onset of steady Bénard-Marangoni convection in a layer of conducting fluid. *Journal of Engineering Mathematics*, 27:161–188, 1993.

107. P. Yecko, S. Zaleski, and J.-M. Fullana. Viscous modes in two-phase mixing layers. *Phys. Fluids*, 14:4115–4122, 2002.

108. O. Zikanov and A. Thess. Direct numerical simulation of forced MHD turbulence at low magnetic Reynolds number. *J. Fluid Mech.*, 358:299–333, 1998.

C Erklärung/Declaration

Ich erkläre hiermit, dass ich die vorliegende Arbeit ohne unzulässige Hilfe Dritter und ohne Benutzung anderer als der angegebenen Hilfsmittel angefertigt habe. Das aus anderen Quellen direkt oder indirekt übernommene Material ist als solches unter der Angabe der Quellen gekennzeichnet. / I hereby declare that I have prepared this work without inadmissible help from others and without using aids apart from those described in the text. All material copied directly or indirectly from other sources has been cited with attribution of the source.

Die folgenden unter den als schriftliche Habilitationsleistung vorgelegten wissenschaftlichen Veröffentlichungen weisen mehrere Autoren auf. Mein eigener Anteil beschreibt sich wie folgt. / The following publications among those presented in this written summary of scientific papers have several authors. My contribution to these papers is described as follows.

[1] T. Boeck, C. Karcher, Low-Prandtl-number Marangoni convection driven by localized heating on the free surface. *Lect. Notes Phys. vol. 628*, 157-175 (2003)

I developed the numerical code and performed all numerical simulations reported in this paper. I also wrote most of the text. My co-author contributed to the introduction and to the review of the scaling theories in section 2.

[4] T. Boeck, A. Thess, Power-law scaling in Bénard-Marangoni convection at large Prandtl numbers. *Physical Review E*, vol. 64, 027303 (2001).

I developed the numerical code and performed all numerical simulations reported in this paper. I also wrote most of the article. The motivation for the study comes from previous work by my co-author, but it was begun on my own initiative. My co-author contributed to the introduction and summary, and to the interpretation of the boundary-layer scaling results.

[5] T. Boeck, A. Nepomnyashchy, I. Simanovskii, Three-dimensional simulations of water-mercury anticonvection. *Fluid Dynamics and Materials Processing*, vol. 4, pp. 11-19 (2008)

The study was begun on my own initiative with the original motivation coming from my co-authors. I used my own numerical code to perform all numerical simulations reported in this paper. I also wrote most of the paper. My co-authors suggested some of the analyses and contributed to the interpretation of the results in the conclusions.

[6] T. Boeck, A. Nepomnyashchy, I. Simanovskii, A. Golovin, L. Braverman, A. Thess, Three-dimensional convection in a two-layer system with anomalous thermocapillary effect. *Physics of Fluids*, vol. 14, 3899 (2002).

The study was begun in the framework of a project funded by the German-Israeli Foundation for Scientific Research and Development, which involved Prof. Thess and myself at TU Dresden and Profs. Nepomnyashchy, Simanovskii and Golovin at the Israeli Institute of Technology in Haifa. It was completed while I was working as a postdoc at the University of Paris. The motivation for the investigation of two-layer convection came from Profs. Nepomnyashchy, Simanovskii and Golovin. I developed the numerical code and performed all numerical simulations reported in this paper. I wrote substantial parts of the paper, including most of sections 2,3, and 4. My co-authors suggested some of the analyses and contributed to the interpretation of the results and to the writing. They also contributed the linear stability results in Fig. 1.

[7] T. Boeck, S. Zaleski, Viscous versus inviscid instability of two-phase mixing layers with continuous velocity profile. *Physics of Fluids*, vol. 17, 032106 (2005).

This study originated from discussions with Prof. Zaleski on viscous effects in the linear instability of two-phase shear layers. I performed all numerical stability computations reported in this paper and wrote most of the text. The linear stability codes had been developed in the group of Prof. Zaleski. I modified them for this study. Prof. Zaleski contributed to the formulation of the mathematical model, to the interpretation of the results, and suggested the comparison with experimental data in section 5.

[8] T. Boeck, S. Zaleski, Instability of two-phase mixing layers: analysis of exact and approximate base flows from boundary layer theory. *J. Noneq. Thermodyn.*, vol. 30(3), pp. 215-224 (2005).

This study was begun on my own initiative using linear stability codes that had been developed in the group of Prof. Zaleski. I peformed all numerical computations reported in this paper and wrote most of the text. Prof. Zaleski contributed to the interpretation of the results.

[9] T. Boeck, P. Yecko, A. Bagué, S. Zaleski, Instability in two-phase mixing layers. Proceedings of the Sixth International Conference on Multiphase Flow, Leipzig, 9-13 July 2007.

This computational study was suggested by Prof. Zaleski during my stay in Paris. I modified the viscosity method and added the initialization with eigenfunctions to the SURFER code, which had been developed by Prof. Zaleski and his co-workers. I performed the simulations with SURFER and the stability computations for this paper. My co-authors contributed to the introduction and to the summary of the paper, and to the interpretation of the results.

[10] T. Boeck, D. Krasnov, E. Zienicke, Numerical study of turbulent magnetohydrodynamic channel flow. *Journal of Fluid Mechanics*, vol. 572, pp. 179-188 (2007).

This computational study continued previous investigations on transition in the Hartmann flow (published in Krasnov et al. Journal of Fluid Mechanics vol. 504, pp.183-211). I developed the original numerical code, and initiated several of the analyses performed in this paper, in particular the comparison of the simulation results with turbulence models. I also suggested the extrapolation of the friction coefficients to infinite Hartmann number, and I wrote the paper.

[11] D. Krasnov, M. Rossi, O. Zikanov, T. Boeck, Optimal growth and transition to turbulence in channel flow with spanwise magnetic field. *Journal of Fluid Mechanics*, vol. 596, pp. 73-101 (2008).

This computational study was begun on my initiative. I developed the original code for the direct numerical simulations. I participated in the formulation of the adjoint equations, and in the development of the code for the optimal perturbations. I also suggested several of the analyses, in particular the scaling analysis of streamwise perturbations. The writing was a joint effort by all authors.

[12] D. Krasnov, O. Zikanov, J. Schumacher, T. Boeck, Magnetohydrodynamic turbulence in a channel with spanwise magnetic field. *Physics of Fluids*, vol. 20, 095105 (2008).

The pseudospectral large-eddy simulations of magnetohydrodynamic channel flow were begun on my initiative. I was involved in the conception of the numerical studies, contributed to the interpretation and analysis of the numerical results, and wrote some sections of the paper.

[13] D. Krasnov, O. Zikanov, J. Schumacher, T. Boeck, Energy dissipation rates in low-Re_m MHD turbulence with mean shear: Results for channel flow with spanwise field. *Magnetohydrodynamics*, vol. 45, pp. 155-164 (2009).

I suggested certain analyses for this numerical study, and contributed to the interpretation of numerical results. I wrote substantial parts of the paper.

[14] T. Boeck, D. Krasnov, A. Thess, O. Zikanov, Large-scale intermittency of liquid-metal channel flow in a magnetic field. *Physical Review Letters*, vol. 101, 244501 (2008).

I was involved in the conception of this numerical study, and contributed to the analyses of numerical results. I also developed the original numerical code used in this study. I wrote large parts of the final paper, which started from a draft prepared

by my co-authors.

Die Arbeit wurde bisher weder im Inland noch im Ausland in gleicher oder ähnlicher Form einem anderen Prüfungsgremium vorgelegt. / This work has not previously been submitted to an examination board in its present or a similar form, neither in Germany nor abroad.

Ilmenau, den 8. 6. 2009

T. Boeck

D Acknowledgments

The publications presented in this work have been prepared at several institutions. As a postdoc at the Max Planck Institute for Physics of Complex Systems in Dresden I have mostly worked on Marangoni flows. My work on two-phase flows at the University of Paris was supported by a postdoctoral research grant from the Deutsche Forschungsgemeinschaft. The Deutsche Forschungsgemeinschaft has also funded my junior research group at the Faculty of Mechanical Engineering of TU Ilmenau in the framework of the Emmy Noether program.

My scientific activities reported in this work would not have been possible without my collaborators. I am grateful to them for stimulating discussions, advice and encouragement. They are (in alphabetical order)

C. Karcher,

D. Krasnov,

A. Nepomnyashchy,

M. Rossi,

J. Schumacher,

I. Simanovskii,

A. Thess,

P. Yecko,

S. Zaleski,

E. Zienicke,

O. Zikanov.

I am especially grateful to Prof. André Thess, who provided essential support for the establishment of my own research group. I also thank Prof. Zaleski and Dr. Rossi for their hospitality and support during my stay at the University of Paris VI. Finally, I thank my parents for their support and encouragement over the years.